



STRONG GRAVITATIONAL LENSING:

CONSTRAINING THE GALACTIC MASS PROFILE

CONOR O'RIORDAN

SUBMITTED 17th SEPTEMBER, 2016

A THESIS SUBMITTED IN PARTIAL
FULFILMENT OF THE REQUIREMENTS FOR
THE DEGREE OF MASTER OF PHYSICS AND
THE DIPLOMA OF IMPERIAL COLLEGE LONDON

DECLARATION

All work submitted here is entirely my own, completed while undertaking the MSc Physics program at Imperial College, London. Where the work of others has aided or influenced me they have been fully credited.

The presented results are genuine and are the output of computer programs written entirely by myself with the use of standard libraries in *Python*. Where results from other authors are used they are fully credited either in the respective figure or in the text.

Schematics were drawn by myself in *Adobe Illustrator* and plots were produced by myself using *Mathematica* and *Python*. Typeset in *LAT_EX* with the *tufte-book* template.

Conor O'Riordan,
September 2016

A B S T R A C T

Strong gravitational lensing is an important tool within many areas of astronomy and cosmology. It provides the most precise measurements of galactic mass, and coupled with dynamical studies, has been used to measure the slope of the total mass distribution, γ with constraints of $\pm 5\%$ to $\pm 10\%$. Although not as common, lensing has been used on its own to constrain γ . However, the limitations of this technique and its dependence on the parameters in the lens and the source are not completely clear.

Using an elliptical lensing model to create and compare simulated images for different parameters, we attempt to establish constraints on the mass profile using lensing alone. By truncating the mass distribution of the lens at a radius within the images, we ensure that image formation is a function only of interior mass distribution, rather than the mass at or between the images. We show that small changes in mass profile and ellipticity produce images that are different enough to place useful constraints on γ , on the order of $\pm 5\%$ or smaller. We also show that the size of these constraints depends on the ellipticity of the lens and the position and size of the source.

Contents

1	Introduction	1
1.1	The Uses of Lensing	2
1.2	Measuring the Mass Distribution	3
1.3	Departing from Dynamics	4
1.4	Motivation	5
2	Lensing Theory	7
2.1	The Thin Lens Approximation	7
2.2	Deflection Angle for the Point Mass	9
2.3	Einstein Radius and Rings	9
2.4	Convergence, Shear and the Magnification Tensor . . .	12
2.5	Degeneracies in Circular Lenses	13
2.6	The Mass Sheet Degeneracy	15
2.7	Elliptical Geometry	15
2.8	Critical Lines, Cuts and Caustics	16
3	Method	19
3.1	Calculating the Deflection Angle	21
3.2	Truncating the Mass Distribution	23
3.3	Implementation and Discretisation	24
3.4	Computation Speed and Optimisation	27
3.5	Defining Sources	28
3.6	Constructing Images	28
3.7	Comparing Images	29
4	Results	31
4.1	Constraints on Total Mass	31
4.2	Constraints on γ at Different Ellipticities	31
4.3	Constraints on γ with Different Source Positions . . .	31
4.4	Constraints on γ with Different Source Sizes	31
5	Discussion and Conclusions	37
5.1	Degeneracies and Validity of Results	37
5.2	Limitations of Method	38
5.3	Statistical Analysis	38
5.4	Summary of Key Results	39

1 Introduction

IN CERTAIN CIRCUMSTANCES, the curvature of space itself becomes a powerful astronomical instrument via the *gravitational lens*. This rare phenomenon occurs when far away photons encounter a massive object along their trajectory. The curvature of space around these objects in the foreground, most often galaxies or galaxy clusters, slightly alters the path of the photons from objects in the background.

If the alignment is right, the obvious consequence is that massive objects can direct photons towards us which we otherwise would never have seen, or might have seen in a different way. On the plane of the sky, the gravitational lens itself is seen surrounded by a number of magnified and deformed images of the background object. Figure 1.1 is a cartoon example of such an alignment.

Observing and understanding these distortions through the gravitational lens has become very important to astronomers and cosmologists alike. This understanding, particularly as it relates to matter at the galactic scale, is the subject of the work presented here.

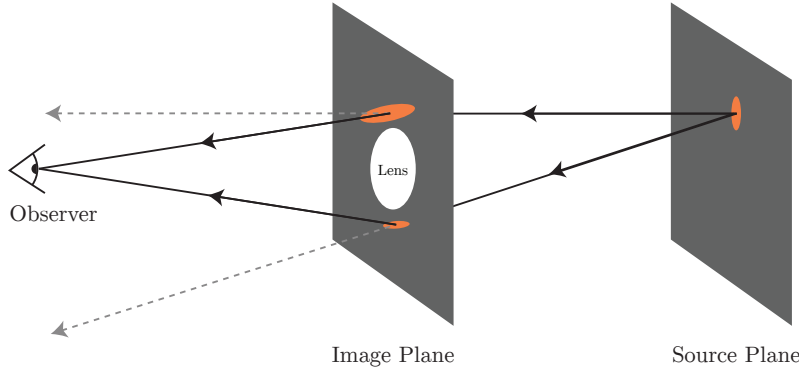


Figure 1.1: A simple schematic of a typical lensing situation. In this example the source is off the optical axis. The deflection of light as it passes the lens is such that two images of the source form, one being slightly magnified.

We observe three distinct forms of lensing; strong, weak and micro. In the strong case, light is deflected to produce multiple images by a galaxy or a galaxy cluster. Most of the known strong lenses are galaxies and it is this specific type of lensing that will be the focus of this work.

Strong lensing was predicted theoretically, as a consequence of general relativity, in the first half of the 20th century. It would be another half a century until the first observations of real strong lenses and to the development of the field of lensing in its own right. The number of lenses with confirmed multiple images now stands at over 100 and as the capability of surveys increases new lenses are discovered with increasing frequency (Shu et al., 2016). What was once a rare phenomenon is now the subject of intense study within cosmology and astronomy.

1.1 The Uses of Lensing

A quick survey of the work to date on lensing would highlight its use in three main areas. Firstly, as the illustration in figure 1.1 might suggest, a gravitational lens often magnifies very distant images. This allows us to study objects which would have been too faint to observe traditionally. Most of the known strong lenses have sources at $1 < z < 3$ and lensing has been used to study the furthest known galaxy at $z = 11$ (Coe et al., 2013). The distribution of lenses in terms of redshift is shown in figure 1.2.

Secondly, over such distances deflections of light are naturally influenced by the cosmology of the universe at large. This aspect of lensing is most often exploited via the time delay between different images of the same source. The delay experienced by light travelling along two different paths depends strongly on the Hubble constant, and weakly on the cosmological mass-density parameters (Linder, 2011). Measuring the delay directly for a time-varying source then allows lensing studies to measure the Hubble constant to an impressive accuracy. Suyu et al. (2010) and Bonvin et al. (2016) demonstrate this with particular success.

Thirdly, the location and orientation of images around a lens de-

Weak Lensing:

Deflection of light on a cosmic scale due to general inhomogeneities, rather than a specific object.

Micro Lensing:

Transient lensing events caused by smaller objects, observed as momentary increases in brightness of background sources.

The first gravitational lens, a doubly imaged quasar was found by [Walsh et al. \(1979\)](#).

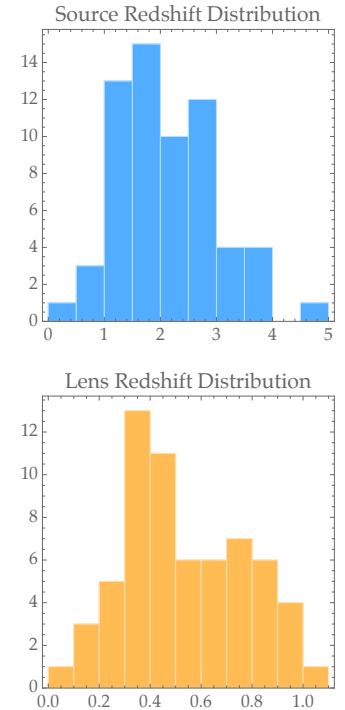


Figure 1.2: The distribution of lenses in source and lens redshift according to the [CASTLES database](#), a database of all multiple image lenses, maintained by Kochanek and others.

pends critically on the amount and distribution of mass within the lens itself. This makes lensing a powerful tool for probing the distribution of both dark and baryonic matter at the galactic and sub-galactic scales. It is this area which has motivated the bulk of the lensing literature so far, and also motivates the work presented here.

Various models exist to recreate the images produced by lenses and these will be discussed in detail later. We can use such a model to find the angle of deflection in a two-dimensional plane surrounding the lens. Given a background source, we can then simulate the entire lensing event and construct an image.

As the theoretical outline in the next chapter will make clear, the form of the image will depend heavily on the distribution of mass within the lens. Changing this distribution will change the images and measuring this change allows us to place statistical constraints on the parameters in the mass distribution.

1.2 Measuring the Mass Distribution

Understanding the distribution of mass within galaxies is an important part of understanding the more general problems of galaxy formation, especially regarding the role of dark matter. It is well known by now that dark matter makes up a large portion of the total mass in a given galaxy. However, less well understood is the interaction between baryonic matter and dark matter that influences structure at the galactic scale and especially how each form of matter is distributed.

Attempting to solve these problems naturally requires highly accurate measurements of the mass within the earliest galaxies. Strong gravitational lensing can provide these measurements and in fact, is the most accurate technique for measuring galactic mass, a claim well argued for by [Courteau et al. \(2014\)](#).

The technique has been in use for some time and was outlined first in [Kochanek \(1991\)](#), showing that strong lensing could constrain galactic masses. More recently, lensing has been combined with galactic dynamics studies to constrain the mass distribution, as well as the total mass. The state of the art on this is the SLACS project, introduced in [Bolton et al. \(2006\)](#). These studies, and most others in the field, assume a density profile for early-type galaxies that follows a simple power law $\rho(r) = r^{-\gamma}$, where the parameter of interest is the slope, γ , such that

$$\frac{d \log \rho}{d \log r} = -\gamma, \quad (1.1)$$

where ρ is the mass density and r is the radial distance from the centre.

Using a combination of strong lensing and dynamics, [Koopmans et al. \(2006\)](#) and [Auger et al. \(2010\)](#) find the average value of the slope within one effective radius to be $\langle \gamma \rangle = 2.078 \pm 0.027$. Using a subset of the same lenses but with improved spectroscopy, [Barnabe et al. \(2011\)](#) find $\langle \gamma \rangle = 2.074 \pm 0.04$.

A galaxy's **effective radius** is a scale length which encloses half of the total light emitted by that galaxy.

The summary result of the SLACS project is that early type galaxies follow a mass density profile with $\gamma \sim 2$ out to at least 100 effective radii. The particular value of 2 for γ means the galaxies closely follow an **isothermal** profile, where the outward thermodynamic pressure balances the inward gravitational collapse, at least theoretically. What makes the result interesting is that this is the **total mass profile** which includes both the baryonic and dark matter components. Separately each component is not well described by a power law at all, but together they can be well described by a very simple law. This puzzling result is often referred to as the ‘bulge-halo conspiracy’ ([Dutton and Treu, 2013](#)).

All of these results rely critically on accurate dynamical techniques being combined with lensing models. The lensing model is used first to measure the total mass within the radius of the images. This is numerically a relatively simple process and involves reconstructing the source and lens to best reproduce the observed image.

The job of lensing in this case is purely to find the total mass and nothing more. This information then forms the basis for the dynamical analysis which constrains the mass profile. The process is detailed in section 3 of [Koopmans et al. \(2006\)](#) but can be summarised in a number of steps:

1. A **spherically symmetric** power law is chosen to describe the total mass profile. The normalisation for this profile is determined from the aforementioned lensing model.
2. The Jeans equations are solved to find the velocity dispersion, with a number of other assumptions therein.
3. After accounting for instrumental effects, the power law model is fit using spectroscopic data to measure the velocity dispersion.

Each of the assumptions above must be justified for the lenses involved, and ultimately the technique relies on accurate velocity dispersion data from spectroscopy which commonly has uncertainties of $\sim 10\%$. It is this velocity dispersion measurement, and its uncertainty, which accounts for most of the uncertainty in the final results. If a constraint on the mass profile could be achieved at the lensing stage, the above assumptions and reliances on other techniques would be unnecessary.

1.3 Departing from Dynamics

The motivation for an approach that does not rely on dynamics should be clear at this stage. Studies using purely lens-modelling techniques for measuring the mass profile are certainly lacking compared to those that incorporate dynamical studies. Nevertheless there are some good examples which we will discuss here.

The best case for a lensing-only analysis is made by [Dye and Warren \(2005\)](#) because it can be directly compared to the dynamic analysis of the same object by [Koopmans and Treu \(2003\)](#). Both stud-

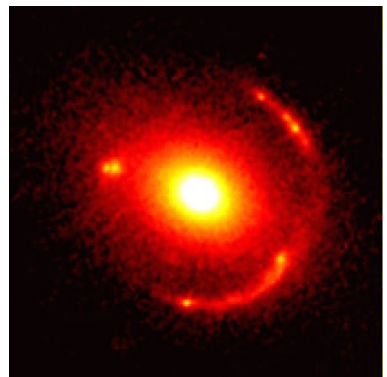


Figure 1.3: An image of the gravitational lens ER-0047-2808 from the Hubble Space Telescope. In the centre is the lens itself, surrounded by 3 images of the source, now known to be two galaxies in the process of merging. Image credit: ESA/NASA

ies consider the strong gravitational lens ER-0047-2808, an image of which is in figure 1.3. Koopmans and Treu follow the technique outlined previously; a lensing model is used to find the total mass within a certain radius and this total mass allows the mass profile to be found via dynamic analysis. Their method finds $\gamma = 1.90^{+0.05}_{-0.23}$.

The analysis in Dye and Warren (2005) is purely based on lensing and uses the ‘semi-linear inversion’ technique first presented in Warren and Dye (2003) and later used as the basis for the analysis in the SLACS papers (Koopmans et al., 2006). It differs from most of the lensing studies before it in that it uses both image **position** and **flux** in the model. As well as this, the source is pixelised with an **adaptive grid** so that there are more pixels in areas with more detail, allowing the maximum amount of image information into the model. In doing so, Dye and Warren find $\gamma = 2.11 \pm 0.04$.

The comparison between these two studies and their results is detailed further in section 1 of Willis et al. (2006) but the clear conclusion is that lensing models can in fact constrain the mass profile on their own, and even to a higher degree of accuracy than a dynamical approach. Treu (2010) expresses scepticism that this is reproducible in general and attributes the result to the “*lensed sources covering a significant radial range*” in this particular case.

The same technique was used again, although slightly modified, in Dye et al. (2007) to measure the properties of the gravitational lens LBG J213512.73-010143. The slope of the total mass profile as a power law was measured to be $\gamma = 2.09 \pm 0.04$. More recently the method was applied to five strong lenses by Dye et al. (2014). Again, similarly accurate measurements of mass profile and other parameters are found from lensing alone and their results are reproduced in figure 1.4.

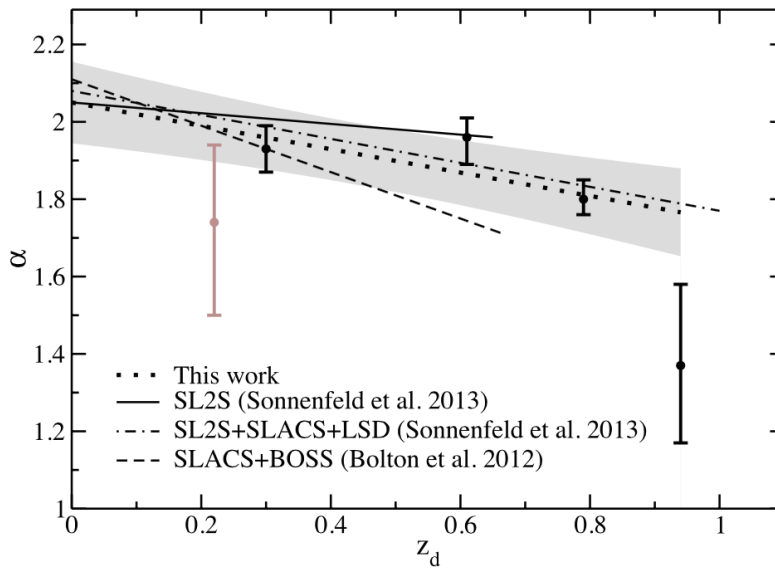


Figure 1.4: The results of a lensing-only analysis of five strong gravitational lenses, compared with results from other studies which combined lensing with dynamical analysis. The different lines show straight line fits between total mass profile slope $\alpha \equiv \gamma$ and the lens redshift z_d . Reproduced from Dye et al. (2014).

1.4 Motivation

There is by now ample evidence that lensing can place strong constraints on the **total mass** of a galaxy. However, the previous section illustrates the persistent uncertainty in the community as to whether lensing alone can constrain the **mass distribution**. Two of the most cited reviews on the matter go so far as to claim it can only be done in very specific circumstances, if at all. For illustration, these reviews are quoted verbatim below.

"Even for these systems, it is important to remember that the actual constraints on the density structure really only apply over the range of radii spanned by the lensed images - the mass interior to the images is constrained but its distribution is not, while the mass exterior to the images is completely unconstrained."

From Kochanek et al. (2004).

"It should be noted that lensing is mostly sensitive to the projected mass-density slope at the location of the images, rather than the average inside the images. Therefore, a direct comparison with the lensing and dynamical results is only valid to the extent that a pure power-law profile is a good model for the data."

From Treu (2010).

As the theory in the next chapter will show, these comments are entirely valid for completely circular lenses. However, in an elliptical lens model, the sensitivities described above are complemented by angular distortion in the images and a breaking of the symmetry which prevents constraints. With more image information available to the model, sensitivities to the mass profile **interior** to the images become apparent.

Turning now to the work at hand, it is precisely this problem which we concern ourselves with; to what extent can the mass distribution of a lens be constrained from lensed images alone?

In order to properly address the issue, the paper is organised as follows. Having now reviewed the literature on the problem so far, chapter 2 will introduce the necessary lensing formalism to deal with the rest of the work. The computational method for constructing and comparing images is detailed in chapter 3. Key results of the study are presented in chapter 4. Finally, we discuss the results and their implications in chapter 5.

2 Lensing Theory

To properly describe a lensing event does not require any particularly advanced physics or mathematics but the theoretical results can often be difficult to visualise. This can make parts of the theory seem abstract or irrelevant at first encounter despite lensing being a very visual phenomenon. As such, the explanation here will be as visual as possible.

The lensing formalism is quite well developed and what follows here is only a brief treatment, although quite adequate for our purposes. The interested reader can supplement the discussion with either of the suggestions in the margin.

2.1 The Thin Lens Approximation

The distances from source to lens, and from lens to observer are many orders of magnitude greater than the extension of the lens along the line of sight. For this reason it is correct and convenient to treat the lens as a two-dimensional object, projected onto a plane called the image plane. This important step is called the *thin lens approximation*. It is on this image plane that we observe the images and the lens itself.

A photon leaves the source plane from an angular position β and strikes the image plane at an angular position θ . When it does so, its path is deflected by an angle $\alpha(\theta)$ which is a function of the mass distribution in the lens and the position on the image plane.

The geometry of the problem is illustrated by figure 2.1. It is important to emphasise here that the lensing problem in general is one of **coordinate transformation**. We observe the positions of the images on the image plane. We can then transform these positions back to the source plane via the geometry in the figure and some information about the mass distribution in the lens, which determines $\alpha(\theta)$.

What is needed then is an equation which describes this coordinate transformation. We start by defining the *reduced deflection angle* as

$$\alpha = \frac{D_{ds}}{D_s} \hat{\alpha} \quad (2.1)$$

and we see from the figure that

$$D_s \theta = D_s \beta + D_{ds} \hat{\alpha}. \quad (2.2)$$

Kochanek et al. (2004) provides a thorough and extensive lecture-style overview and the explanations of **caustic structure** therein are especially relevant to this work.

Naryan and Bartelmann (1995) gives a concise summary of all the essential concepts in a shorter format with less emphasis on the results from lensing studies.

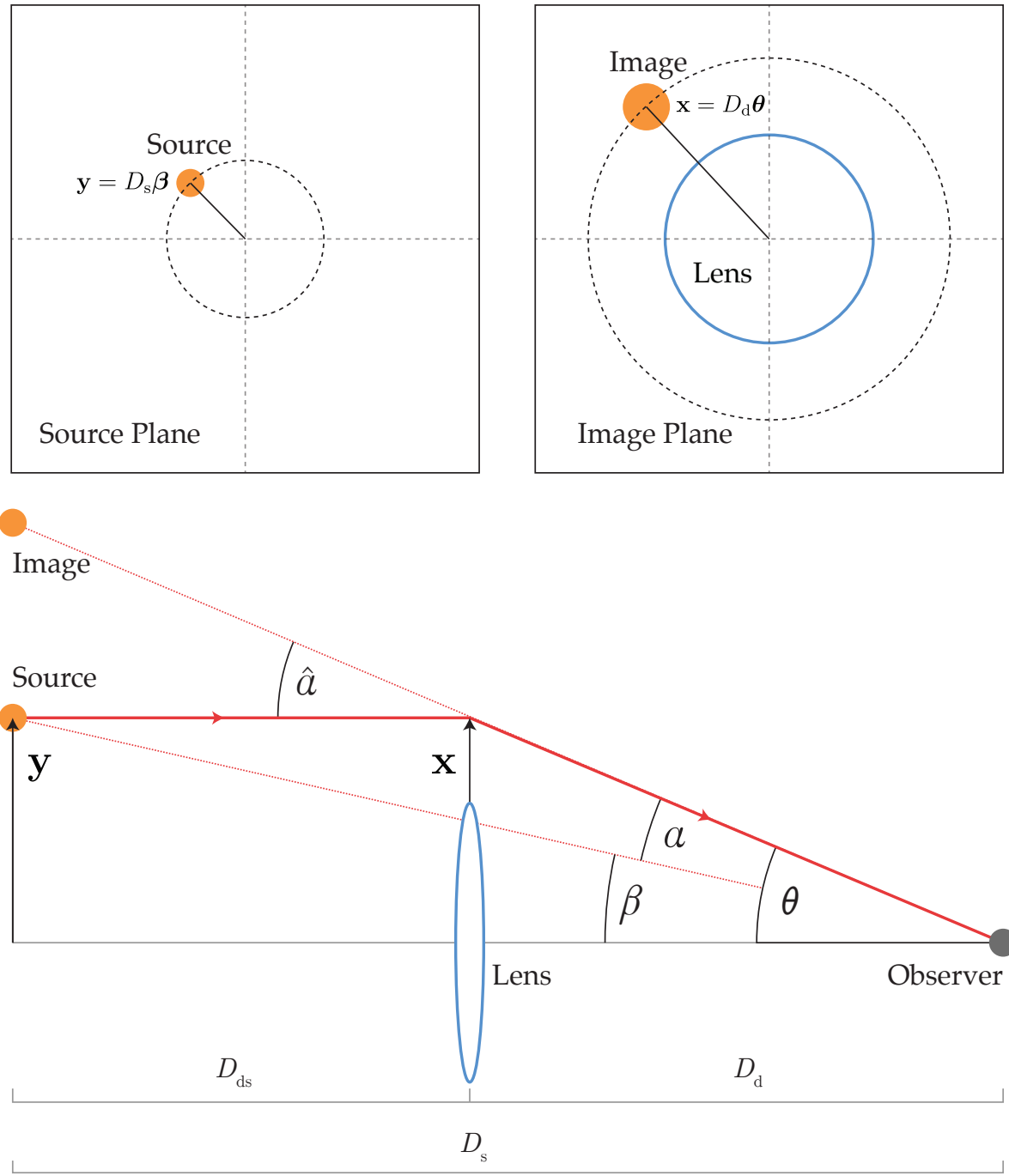


Figure 2.1: The geometry of a typical gravitational lensing event. A photon leaves the source at a position $y = D_s \beta$ and strikes the image plane at a position $x = D_d \theta$ where it is deflected by an angle $\alpha(\theta)$ and forms an image. D_{ds} , D_s and D_d are the distances from lens to source, from source to observer, and from observer to lens respectively.

Eliminating $\hat{\alpha}$ with the above gives us

$$\beta = \theta - \alpha(\theta). \quad (2.3)$$

Equation 2.3 is known as the **lens equation** and in some form or another is the basis for any lensing model.

2.2 Deflection Angle for the Point Mass

To fully solve the lens equation and find the location of a source and its images, we need to calculate $\alpha(\theta)$. Borrowing a result from general relativity, the deflection angle is given by the integral along the path of light of the gradient of the gravitational potential of the lens perpendicular to the path of light, or

$$\hat{\alpha} = \frac{2}{c^2} \int dl \nabla_{\perp} \Phi \quad (2.4)$$

For a simple illustrative example, let us consider a point mass. Its potential is given by

$$\Phi(\mathbf{x}, z) = -\frac{GM}{\sqrt{|\mathbf{x}|^2 + z^2}} \quad (2.5)$$

where \mathbf{x} is a two-dimensional vector describing the position at which the light ray hits the image plane, also called the **impact parameter** (see fig. 2.1) and z is the coordinate along the line of sight, with the origin in the image plane. This yields a deflection angle of

$$\hat{\alpha} = \frac{4GM}{c^2 |\mathbf{x}|} \quad (2.6)$$

¹ or in the more useful form

$$\alpha = \frac{4GM}{c^2} \frac{D_{ds}}{D_s} \frac{1}{|\mathbf{x}|}. \quad (2.7)$$

The deflection angle vector field for the point mass is plotted in figure 2.2.

2.3 Einstein Radius and Rings

Consider again the point mass, we note from figure 2.1 that $\mathbf{x} = D_d \theta$. Exploiting the circular symmetry also allows us to write $|\mathbf{x}| = D_d \theta$ where θ is now simply the radial angular separation between the optical axis and a point on the image plane. The deflection angle at an angular radius θ is now given by

$$\alpha = \frac{4GM}{c^2} \frac{D_{ds}}{D_d D_s} \frac{1}{\theta} \quad (2.8)$$

and the lens equation for the point mass becomes

$$\beta = \theta - \frac{4GM}{c^2 \theta} \frac{D_{ds}}{D_d D_s} \quad (2.9)$$

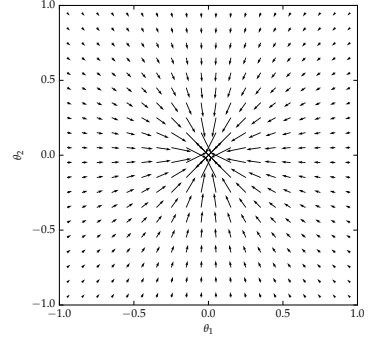


Figure 2.2: The deflection angle vector field for a point mass on the image plane. At any point on the plane, the magnitude and direction of each vector points to its corresponding position on the source plane.

¹ Compare this result with the **Schwarzschild Radius** $R_S = 2GM/c^2$ and we see that the deflection angle for a point mass is simply twice the inverse of the impact parameter in units of R_S , scaled by the distances.

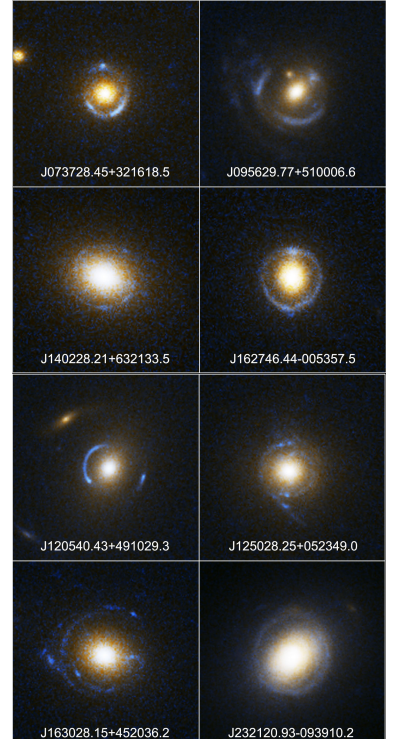


Figure 2.3: Eight examples of real Einstein rings. In each case the bright red/orange central object is the foreground galaxy which has deflected the light from the blue background objects to form the image. Compare these with the image structure in the simulation of fig. 2.4.

Now we define the **Einstein radius** θ_E to be

$$\theta_E^2 = \frac{4GM}{c^2} \frac{D_{ds}}{D_d D_s} \quad (2.10)$$

and we can rewrite the lens equation as

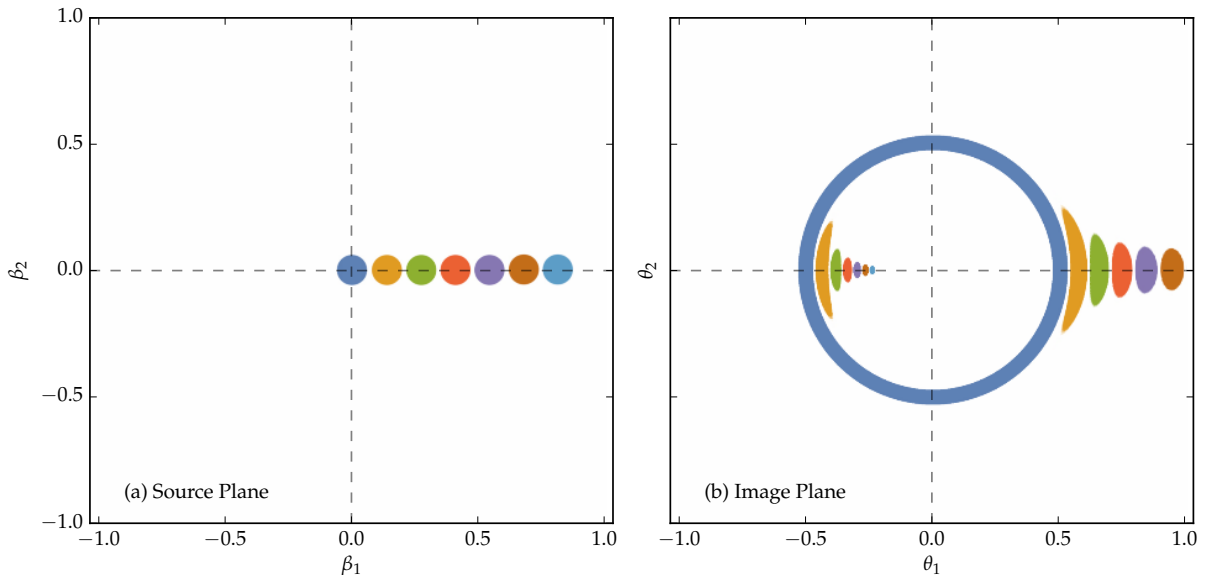
$$\beta = \theta - \frac{\theta_E^2}{\theta} \quad (2.11)$$

If we consider a source on the optical axis, so that $\beta = 0$, equation 2.11 yields two image positions at $\theta = \pm\theta_E$. The circular symmetry here means this image forms at the same radius θ_E all around the lens in an object called an **Einstein ring**. Different source positions form images at different locations, with different properties inside, outside, and on the Einstein ring. This behaviour is simulated in figure 2.4 and for illustration there are examples of real Einstein rings in figure 2.3.

The solutions in θ to equation 2.7 for an arbitrary β are

$$\theta_{\pm} = \frac{1}{2} \left(\beta \pm \sqrt{\beta^2 + 4\theta_E^2} \right) \quad (2.12)$$

which shows two image positions for a given source position, one inside and one outside the Einstein radius. In the extremes, as $\beta \rightarrow 0$, $\theta \rightarrow \pm\theta_E$ and as $\beta \rightarrow \infty$, $\theta \rightarrow \beta$, so far away from the lens we see the source undistorted in its original position.



The distortion and magnification of the images is less clear but a different kind of graphical representation can explain this. Figure 2.5 plots two functions of θ ; the deflection angle θ_E^2/θ and the image position minus the source position $\theta - \beta$. From equation 2.7 we see that images will form at the points where these functions meet. By considering sources extended over a small range $\beta = \beta_0 \pm 0.1$ we see that images outside the Einstein ring are magnified more than

Figure 2.4: Different source positions and the images they produce for a point mass. The deflection angle field used here is that in fig. 2.2. As the source moves away from the optical axis and β increases, the solutions to the lens equation change. The lens equation always has two solutions in θ and so two images are always produced for this lens, either: one inside and one outside θ_E or, one continuous image at θ_E called an Einstein ring (blue).

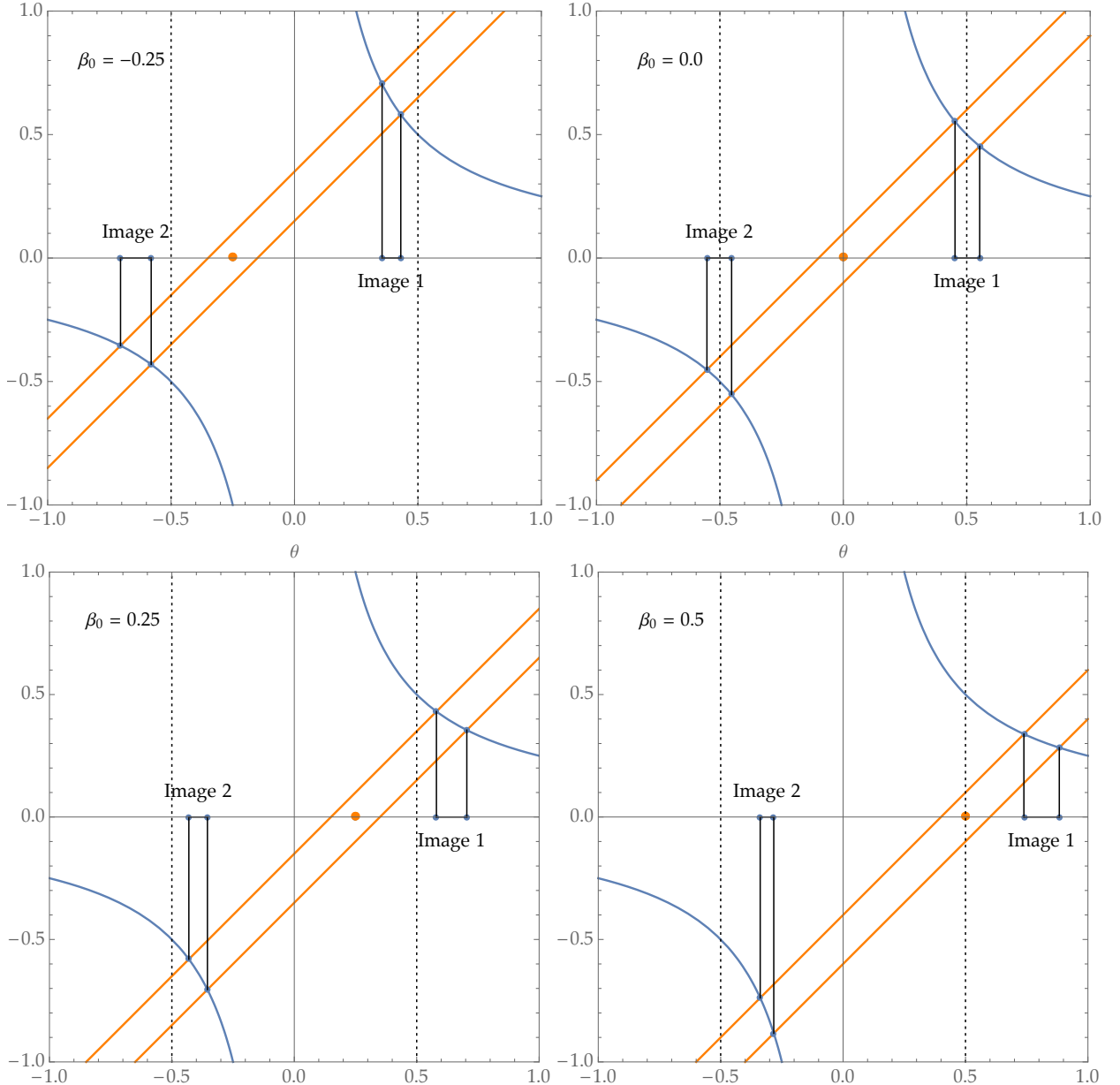


Figure 2.5: The roots of the lens equation for four different source positions with sources extended by 0.1 in either direction. Images form at the roots of the lens equation. The blue lines are the deflection angle θ_E^2/θ and the orange lines are the image position minus the source position $\theta - \beta$. The Einstein radius is the dashed line at $\theta_E = 0.5$. Images with $\theta > \theta_E$ are strongly magnified while images at $\theta < \theta_E$ are weakly magnified.

those inside it. The figure describes magnification in the radial direction, but a similar magnification occurs in the tangential direction, something more obvious in figure 2.4.

2.4 Convergence, Shear and the Magnification Tensor

In this section we develop the lensing formalism much further. Many of the terms defined here are not strictly necessary for discussing the method in the next section, however, we can use the more complicated lensing concepts to make a crucial point that will be quite relevant later: that elliptical lenses provide much more information (and tighter constraints) in their images than circular ones.

Departing now from the point mass of the previous sections, we define a general three-dimensional mass distribution $\rho(\mathbf{x}, z)$ and project it onto the image plane to obtain a two-dimensional mass distribution $\Sigma(\mathbf{x})$ via the integral

$$\Sigma(\mathbf{x}) = \int dz \rho(\mathbf{x}, z). \quad (2.13)$$

The deflection angle at a point \mathbf{x} is now given by integrating over the contributions to deflection from each element of mass in the image plane:

$$\hat{\alpha}(\mathbf{x}) = \frac{4G}{c^2} \int d^2x' \Sigma(x') \frac{\mathbf{x} - \mathbf{x}'}{|\mathbf{x} - \mathbf{x}'|^2} \quad (2.14)$$

We can simplify the expression above by defining two new quantities to describe the mass distribution, the **critical density** Σ_{cr} , and the **convergence** $\kappa(\mathbf{x})$ as such:

$$\Sigma_{\text{cr}} = \frac{c^2}{4\pi G} \frac{D_s}{D_d D_{ds}} \quad \kappa(\mathbf{x}) = \frac{\Sigma(\mathbf{x})}{\Sigma_{\text{cr}}}, \quad (2.15)$$

which lets us rewrite the deflection angle as

$$\alpha(\theta) = \frac{1}{\pi} \int d^2\theta' \kappa(\theta') \frac{\theta - \theta'}{|\theta - \theta'|^2}. \quad (2.16)$$

The convergence also defines the **lensing potential**, $\Psi(\theta)$ via

$$\Psi(\theta) = \frac{1}{\pi} \int d^2\theta' \kappa(\theta') \ln |\theta - \theta'| \quad (2.17)$$

which is the traditional gravitational potential of the lens $\Phi(\mathbf{x}, z)$ projected onto the image plane and scaled according to the critical density.

Recall now the idea from section 2.1 that lensing is best thought of as a coordinate transformation. Having found the route of the transformation via the lens equation and the deflection angle, we can define the **Jacobian matrix** \mathbf{A} , for the mapping between the image plane and source plane by differentiating the lens equation in terms of θ :

$$\mathbf{A} = \frac{\partial \beta}{\partial \theta} = \delta_{ij} - \frac{\partial^2 \Psi(\theta)}{\partial \theta_i \partial \theta_j} = \delta_{ij} - \Psi_{ij}, \quad (2.18)$$

The discussion in this section mostly follows the introduction to the more advanced lensing concepts from [Naryan and Bartelmann \(1995\)](#).

where we have defined the partial derivative of Ψ in terms of θ_i and θ_j as Ψ_{ij} . The Jacobian also defines the **magnification tensor** \mathbf{M} with $\mathbf{A} = \mathbf{M}^{-1}$ and defines the scalar magnification via $\mu = \det \mathbf{M}$.

Using two combinations of Ψ_{ij} we can further define the **shear**, η , as

$$\eta_1(\theta) = \frac{1}{2}(\Psi_{11} - \Psi_{22}) \quad (2.19)$$

$$\eta_2(\theta) = \Psi_{12} = \Psi_{21} \quad (2.20)$$

Finally we can rewrite the Jacobian as

$$\mathbf{A} = \begin{pmatrix} 1 - \kappa - \eta_1 & -\eta_2 \\ -\eta_2 & 1 - \kappa + \eta_1 \end{pmatrix}. \quad (2.21)$$

We see now that the distortion of an image is some combination of two effects; the convergence κ and the shear η . Rewriting \mathbf{A} in a different form makes this even more clear

$$\mathbf{A} = (1 - \kappa) \begin{pmatrix} 1 & 0 \\ 0 & 1 \end{pmatrix} - \eta \begin{pmatrix} \cos 2\varphi & \sin 2\varphi \\ \sin 2\varphi & -\cos 2\varphi \end{pmatrix} \quad (2.22)$$

where $\eta^2 = \eta_1^2 + \eta_2^2$ and φ is the angle between the position on the image plane \mathbf{x} and the x -axis. Convergence acting alone causes the isotropic magnification of an image. Shear introduces angular distortion via its non-zero terms in the 12 and 21 components of \mathbf{A} . These effects are illustrated in figure 2.6.

2.5 Degeneracies in Circular Lenses

We can now return to task at hand; constraining the mass distributions of galaxies via models built on the formalism outlined so far. Section 1.2 showed that lensing so far has had success in measuring total mass, but not mass distribution. An assumption of circular symmetry is usually a starting point of the studies in section 1.2 and we show here why this prevents a constraint on the mass distribution.

Consider a circular lens with two images at θ_A and θ_B . We know the images are from the same source position so we can write

$$\beta = \theta_A - \alpha(\theta_A) = -\theta_B + \alpha(\theta_B). \quad (2.23)$$

Assuming a power law mass profile in three dimensions $\rho(r) = r^{-\gamma}$, Kochanek et al. (2004) shows that the deflection angle is given by

$$\alpha(\theta) = \theta_E^{\gamma-1} \theta^{2-\gamma} \quad (2.24)$$

where θ_E is the Einstein radius (the radius of the tangential critical curve) and α points always towards the centre of the lens. We can use the lens equation with the deflection angle to find the Einstein

We use η for the shear instead of the traditional γ to avoid confusion with the slope of the mass profile.

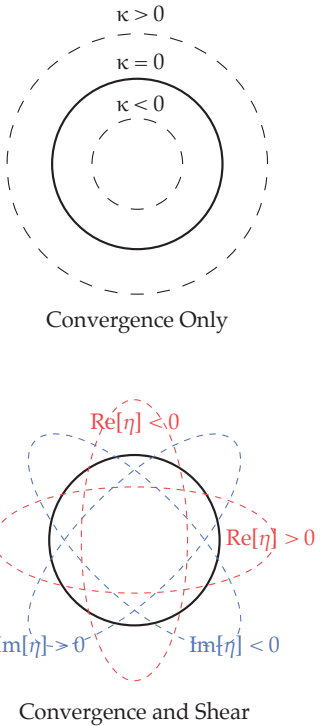


Figure 2.6: The different effects of convergence and shear on an image. The solid circle represents an unperturbed circular source. The dashed lines show the distortion and magnification of the image for different amounts of κ and γ .

radius of the lens as

$$\theta_E = \left(\frac{\theta_A + \theta_B}{\theta_A^{2-\gamma} + \theta_B^{2-\gamma}} \right)^{1/(\gamma-1)} \quad (2.25)$$

There is still a degeneracy between the Einstein radius θ_E and the mass profile slope γ . We can develop this by writing the deflection angle in terms of the convergence and splitting into contributions from inside and outside the inner image θ_B . Again from Kochanek et al. (2004) we see that

$$\alpha(\theta) = \frac{2}{\theta} \left[\int_0^{\theta_B} d\theta' \kappa(\theta') \theta' + \int_{\theta_B}^{\theta} d\theta' \kappa(\theta') \theta' \right] \quad (2.26)$$

The first integral gives the Einstein radius of the mass interior to image B, $\theta_{E_B}^2$. The second integral gives the mean surface density of the mass in the annulus $\theta_B < \theta' < \theta$. The deflection angle becomes

$$\alpha(\theta) = \frac{1}{\theta} \left[\theta_{E_B}^2 + (\theta^2 - \theta_B^2) \langle \kappa \rangle(\theta, \theta_B) \right]. \quad (2.27)$$

We now use this to solve the constraints on source position in equation 2.23 and obtain

$$\theta_{E_B}^2 = \theta_A \theta_B - \langle \kappa \rangle_{AB} (\theta_A - \theta_B) \quad (2.28)$$

where $\langle \kappa \rangle_{AB}$ is the mean mass density in the annulus $\theta_B < \theta < \theta_A$. This shows that the degeneracy here is between the **total mass inside θ_B** and **the mean surface density between θ_B and θ_A** . Clearly, there is no dependence on the mass distribution inside θ_B or between θ_B and θ_A . Neither is there any dependence on the total mass or mass distribution outside θ_A .

All of the constraint equations here are in one dimension and have been easy to calculate because all images lie on a line that passes through both the source and the centre of the lens. The total symmetry of the circular lens at once simplifies the problem and adds tremendous difficulty.

This degeneracy inherent in the circular lens begins to break when we depart from circular symmetry and consider elliptical lenses. As will be shown in the rest of this chapter, elliptical lenses exhibit much greater complexity in their image structure.

Our method will exploit this fact to constrain the mass distribution within the radius of the images by using an elliptical model which breaks the symmetries of the circular lens and adds complicated angular structure to the images, from which a model can extract a greater amount of information.

This is coupled with a **truncation of the mass distribution** at a radius well inside the images. By normalising the total mass for different distributions, the images depend only on the mass distribution inside the lens.

2.6 The Mass Sheet Degeneracy

There is another more general degeneracy which can cause difficulty for lens modelling. The full derivation can be found in Falco et al. (1985) but the key result is that a transformation of the mass distribution

$$\kappa(\theta) \rightarrow \kappa'(\theta) = \lambda\kappa(\theta) + (1 - \lambda) \quad (2.29)$$

combined with a transformation of source position

$$\beta \rightarrow \beta' = \lambda\beta \quad (2.30)$$

leaves the image positions and flux ratios of the images unchanged. That is to say; adding a sheet of constant mass to the image plane and moving the source at the same time can produce identical image structures. The changes in mass distribution under the transformation are shown in figure 2.7. This is known as the **mass-sheet degeneracy** and its origins and methods for breaking it are discussed in Schneider and Sluse (2013).

2.7 Elliptical Geometry

To properly answer the questions introduced in section 1 we will need to account for the fact that circular symmetry is not a general property of galaxies. Also as we have seen, an assumption of circular symmetry makes it impossible to constrain the mass profile without auxiliary information about the lens.

Much of the rest of the paper will be discussed in terms of elliptical geometry so a few necessary terms are defined here. Firstly, an ellipse is defined as a curve surrounding two focal points, such that the sum of the distance to each focal point from each point on the curve is the same. On the image plane we can define it with the parametric equation

$$\frac{x_1^2}{a^2} + \frac{x_2^2}{b^2} = 1. \quad (2.31)$$

where $\mathbf{x} = (x_1, x_2)$ and a and b are the semi-major and semi-minor axes of the ellipse, the points of intersection between the ellipse and each axis, and $a > b, b > 0$. Defining the axis ratio $f = b/a$ allows us to define an **elliptical radius** ζ :

$$\zeta^2 = x_1^2 + f^2 x_2^2. \quad (2.32)$$

This is essentially a normal radial coordinate, but one of the components is scaled by the axis ratio. Contours of constant ζ are called **homoeoids**. We can parameterise a set of homoeoids with m via the equation

$$\frac{x_1^2}{(ma)^2} + \frac{x_2^2}{(mb)^2} = 1. \quad (2.33)$$

For all $m > 0$ the ellipses have the same axis ratio f but **not** the same foci. To define a set of ellipses that share the same focal points we

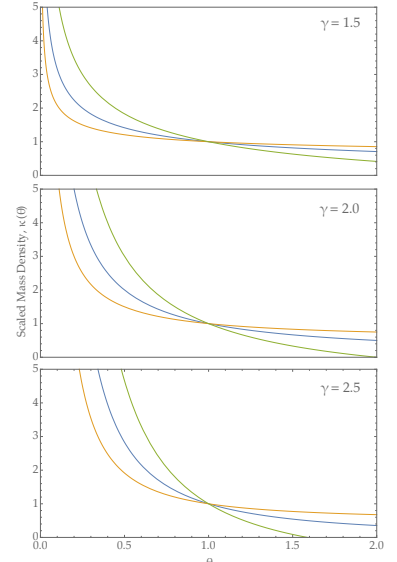


Figure 2.7: The effect of the mass sheet degeneracy for power law mass profiles with $\kappa(\theta) = \theta^{1-\gamma}$. For each γ , $\kappa'(\theta)$ is plotted for $\lambda = 0.5, 1.0$ and 2.0 .

can instead parameterise with λ and obtain

$$\frac{x_1^2}{a^2 + \lambda} + \frac{x_2^2}{b^2 + \lambda} = 1. \quad (2.34)$$

For all $\lambda > 0$ each ellipse shares the same focal points and as $\lambda \rightarrow \infty$ the confocal becomes a circle. The distinction is made clearer in figure 2.8 and will be important when we discuss the deflection angle in elliptical lenses.

2.8 Critical Lines, Cuts and Caustics

Having established that elliptical considerations are necessary, we return now to the discussion of image structure and interpretation, picking up from sections 2.3 and 2.4.

The eigenvalues of the Jacobian, \mathbf{A} for a spherical lens are given by $\lambda_+ = 1 - \kappa - \eta$ and $\lambda_- = 1 - \kappa - \eta$. Their corresponding eigenvectors point in the radial and tangential directions. The points on the image plane where $\lambda_+ = 0$ or $\lambda_- = 0$ form the radial and tangential **critical curves**. On these curves the magnification \mathbf{M} diverges. As such, the critical curves separate the different regimes of magnification on the image plane.

In a spherical lens, an image on the tangential critical curve will become infinitely magnified in the tangential direction and form an Einstein ring. The critical curve then is the generalisation of the Einstein radius to more complicated lens shapes.

If the critical line divides different regimes of distortion on the image plane, then we can project the curve onto the source plane via the typical process, with which by now we are quite familiar. The projection of the tangential critical line onto the source plane is called the **caustic**.

To illustrate the utility of dealing with caustic structure we use an elliptical, isothermal mass profile with $\gamma = 2$, an axis ratio $f = b/a$, an ellipticity $\epsilon = 1 - f$ and a mass distribution of $\kappa(\zeta) = \zeta^{-1}$. This particular profile is called the **single isothermal ellipsoid** (SIE) and Kormann et al. (1994) provides analytic solutions for most of the properties of this lens.

The components of the deflection angle vector are given by

$$\alpha_1 = -\frac{\sqrt{f}}{f'} \operatorname{arcsinh} \left(\frac{f'}{f} \cos \varphi \right) \quad (2.35)$$

$$\alpha_2 = -\frac{\sqrt{f}}{f'} \operatorname{arcsin} (f' \sin \varphi) \quad (2.36)$$

where again φ is the angle between the vector \mathbf{x} on the image plane and the x -axis and $f' = \sqrt{1 - f^2}$. The Jacobian is given by

$$\mathbf{A} = \begin{pmatrix} 1 - 2\kappa \sin^2 \varphi & \kappa \sin 2\varphi \\ \kappa \sin 2\varphi & 1 - 2\kappa \cos^2 \varphi \end{pmatrix}. \quad (2.37)$$

The critical curve is given by $\det \mathbf{A}(\theta) = 0$. Solving the lens equation

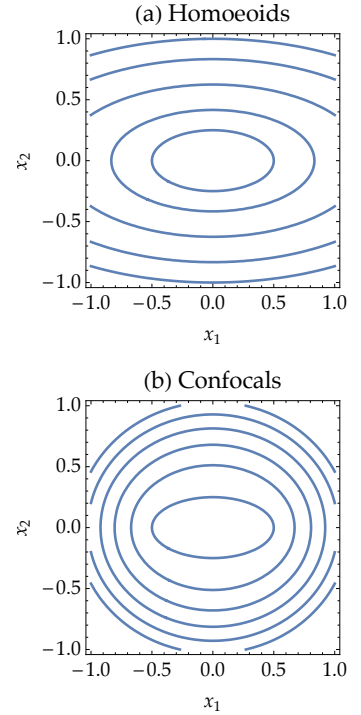


Figure 2.8: Confocal and homoeoidal sets of ellipses for an original ellipse with $a = 0.50$, $b = 0.25$. Note the way the confocals keep their ellipticity whereas the homoeoids eventually become circles.

(eq. 2.3) with the deflection angle above gives a parametric solution for the caustic

$$\beta_1 = \frac{\sqrt{f}}{\Delta(\varphi)} \cos(\varphi) - \frac{\sqrt{f}}{f'} \operatorname{arcsinh} \left(\frac{f'}{f} \cos \varphi \right) \quad (2.38)$$

$$\beta_2 = \frac{\sqrt{f}}{\Delta(\varphi)} \sin(\varphi) - \frac{\sqrt{f}}{f'} \operatorname{arcsin} (f' \sin \varphi) \quad (2.39)$$

where

$$\Delta(\varphi) = \sqrt{\cos^2 \varphi + f^2 \sin^2 \varphi}. \quad (2.40)$$

Figure 2.10 shows the images, critical lines, **cuts** and caustics for eight different axis ratios. As a projection of the critical line, the caustic defines the area on the source plane which will produce multiple images on the image plane.

However, because of the singularity of mass at the centre of our SIE lens model, another area outside the caustic also produces multiple images. The curve enclosing this area is called the **cut**. The cut would become the caustic if we added a **core radius** to the model and can be thought of as the limiting case for a caustic with a vanishing core radius.

The location of the cut is then given by the limit

$$\beta_{\text{cut}} = \lim_{\theta \rightarrow 0} \beta(\theta) = -\alpha(\theta) \quad (2.41)$$

which can be found trivially from the solutions to the deflection angle. Let us now interpret the complicated image structure we see in figure 2.10. The image structure follows a set of general rules as follows; sources that cover the caustic will form a ring on the critical line (source A in plots I and II). Sources that are completely enclosed by the caustic will be imaged four times (sources A and B in plot V). Sources outside the caustic but inside the cut will be imaged twice (sources C, D, E, F and G in plot IV). Sources outside the cut will be imaged once (sources F, G and H in plot VIII). These rules are illustrated generally in figure 2.9.

The magnification of each image will depend on its proximity to the critical line. There is formally infinite magnification on the critical line, zero magnification at the centre of the lens and magnification of unity far from the lens.

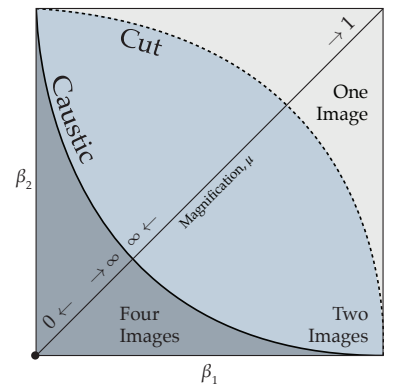


Figure 2.9: An illustration of the image structure in the first quadrant of the source plane. The cut and caustic separate the source plane into three different imaging regimes. The diagonal line across the centre shows the change in scalar magnification as a source moves along the line.

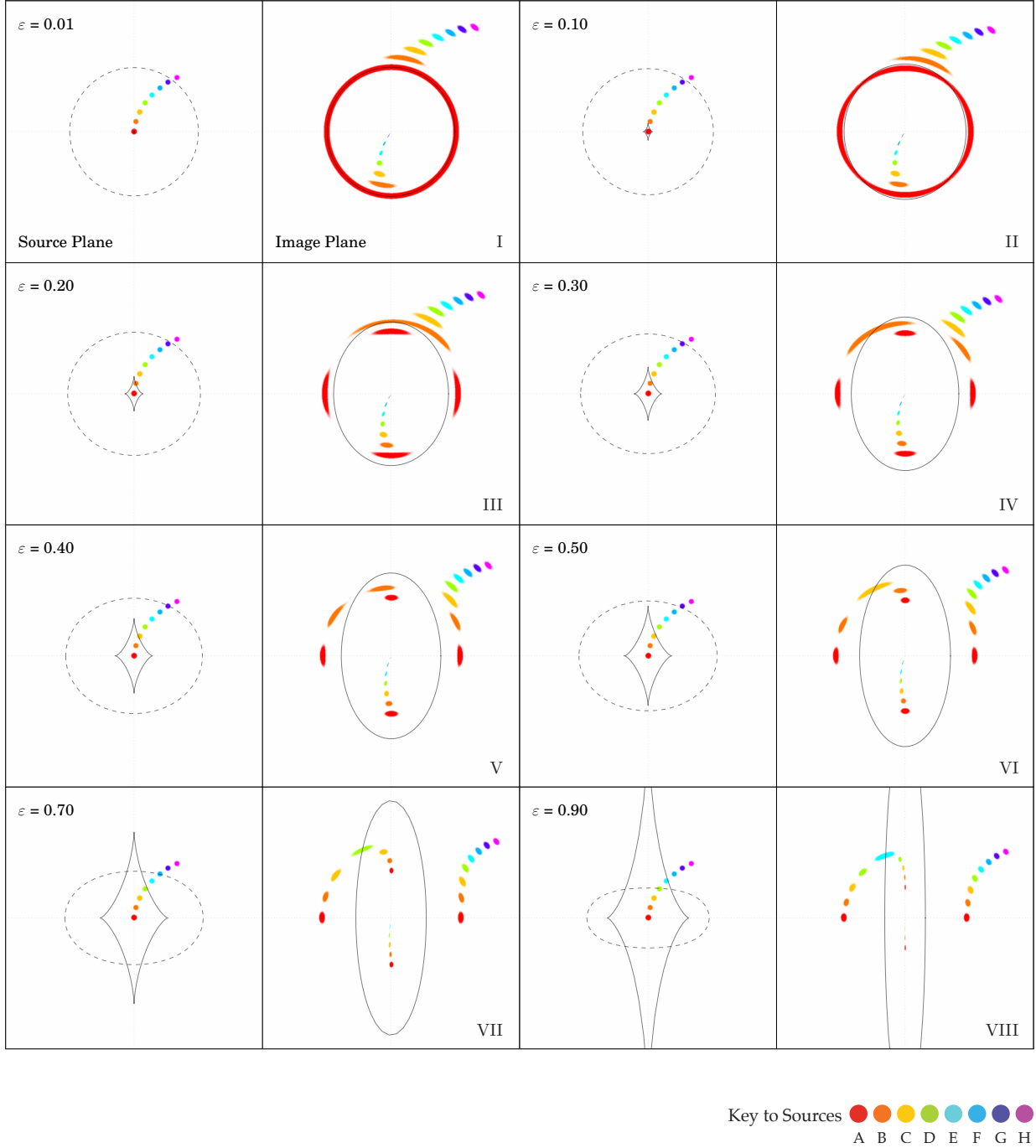


Figure 2.10: The structure of critical lines, caustics and cuts for elliptical lenses. For a given ellipticity, the solid line on the source plane is the tangential critical line. The solid line on the source plane is the caustic. The cut is plotted as a dashed line.

3 Method

To examine the possible constraints on the mass profile from lensing, a method was developed comprising four distinct steps:

1. Define a lens with a power law mass distribution and a source with some light profile.
2. Divide the lensing plane into pixels. In each pixel, calculate the deflection angle by integrating over the mass in the plane.
3. Use the lens equation to trace a light ray from the observer, through the lens, to the source, constructing an image pixel by pixel.
4. Change the parameters and construct a new image, quantifying the difference in image across the parameter space.

Steps one and three are reasonably simple and will require only a short explanation. The bulk of the computation takes place in steps two and four and these steps will take up most of the discussion in this section.

The full routine was written in Python and its NumPy and SciPy libraries lend themselves well to dealing with grids¹. Most of the operations in these libraries are **vectorised**, allowing large arrays (e.g. the grid of pixels) to be used in algebraic expressions. This minimised the need for loops in the bulk of the calculations and provided a fast and lightweight routine.

Before we explain the method, it will be useful to define all the parameters which are used as inputs to the model and their notation. Table 3.1 lists these definitions.

For the rest of the paper, we take a three-dimensional elliptical power law profile defined by $\rho(\zeta) = \zeta^{-\gamma}$ and project it onto the image plane via equation 2.13 so that in two dimensions it becomes $\kappa(\zeta) = \zeta^{1-\gamma}$. The isodensities of this profile are ellipses of constant ζ called **homoeoids** (see fig. 2.8). The approach we will use here is to consider the deflection angle contribution from each of these homoeoids and sum them to find the total deflection angle field on the plane of the lens. Each homoeoid has a homogeneous, constant mass density across it.

¹ SciPy is the umbrella package for scientific computing in Python. NumPy is the part of this package specifically for dealing with operations on large arrays. SciPy also includes matplotlib with which most of the plotting in the rest of the paper was done. Full documentation for all libraries is available at <http://docs.scipy.org/doc/>.

Parameter	Notation	Domain	Comment
Lens Parameters			
Mass Profile Slope	γ	$1.0 < \gamma < 3.0$	The slope of the power law mass profile defined in the previous chapters. $\gamma = 2$ gives an isothermal ellipsoid. $\gamma = 1$ gives a flat mass sheet and $\gamma \rightarrow 3$ approaches the behaviour of a point mass.
Axis Ratio/Ellipticity	f, ε	$0.0 < f, \varepsilon \leq 1.0$	These two parameters define the same thing with $\varepsilon = 1 - f$. In derivations and computer code the axis ratio is much more convenient but in plotting ellipticity is used as it puts the change from circular to elliptical lenses in the positive direction.
Bounding Radius	$\zeta_0 = \sqrt{ab}$	$0.0 < \zeta_0$	The radius after which the mass distribution is set to zero. The semi-axes of the ellipse a and b are set such that the geometric mean of the semi-axes is constant across different axis ratios.
Total Mass	M	$0.0 < M$	The total mass enclosed by the bounding ellipse, after the truncation of the mass profile. This is essentially a normalisation factor which sets the location of the critical line in the image plane.
Source Parameters			
Source Position	$\mathbf{s} = (s_1, s_2)$	$-1.0 < s_1, s_2 < 1.0$	The point on the source plane around which source light profiles are centred.
Source Width	w	$0.0 < w$	The extent of the source's light profile. This could define the radius of a uniformly bright disk, the extent of a cone shaped source, or the width of a Gaussian light profile.
Resolution	N	$50 < N < 500$	The number of pixels along one side of the first quadrant on the image plane. The total pixels on the final image is then $4N^2$.

Table 3.1: The various parameters input to the model, their notation in this text, their domain and comments on their use. The domains are not mathematically exhaustive ones, rather the domains on which they have been used in this work. The presence of absence of trailing decimals indicate floating point or integer definitions.

As the width of the homoeoids $\Delta\zeta$ becomes infinitesimally small, the sum of contributions becomes an integral and we obtain the solution to the deflection angle over the entire lens. This is the method first introduced by Schramm (1990) and expanded upon in Schramm (1994). Significant modifications were then made by Barkana (1998). Ideas from all three papers influenced the method here but ultimately Barkana's calculations produce the final results.

3.1 Calculating the Deflection Angle

Schramm (1990) begins with the gravitational properties of homoeoids, as found by Chandrasekhar (1969) and listed here:

1. The (gravitational) attraction at any internal point of a homogeneous thin **homoeoid** is **zero**. We will label this homoeoid \mathcal{H} .
2. The equipotential surfaces external to \mathcal{H} are ellipsoids **confocal** to \mathcal{H} .²
3. The potential Φ , in three-dimensions, of \mathcal{H} with mass m at a point \mathbf{x} external to \mathcal{H} is given by

$$\Phi = -\frac{GM}{2} \int_{\zeta(\mathbf{x})}^{\infty} du \frac{1}{\sqrt{(a^2 + u)(b^2 + u)(c^2 + u)}} \quad (3.1)$$

where $\zeta(\mathbf{x})$ is the elliptical radius at \mathbf{x} .

From here we can follow the methods in the previous chapter, eventually finding the deflection angle around the slice \mathcal{H} to have the components

$$\alpha_1(\theta_1, \theta_2) = -\frac{2GM}{c^2} \frac{2p'^2}{a'b'} \frac{\theta_1}{a'^2} \quad (3.2)$$

$$\alpha_2(\theta_1, \theta_2) = -\frac{2GM}{c^2} \frac{2p'^2}{a'b'} \frac{\theta_2}{b'^2} \quad (3.3)$$

where $a'^2 = a^2 + \lambda$ and $b'^2 = b^2 + \lambda$ are the semi axes of the ellipsoid which passes through $\Theta = (\theta_1, \theta_2)$ and is confocal to \mathcal{H} which has semi axes a and b . p is a parameter describing the length of the line from the centre to a point on the homoeoid and is given by

$$\frac{1}{p^2} = \frac{\theta_1^2}{a^4} + \frac{\theta_2^2}{b^4} \quad (3.4)$$

and p' is defined using a' and b' in place of a and b . The total deflection angle is then an integral over the contributions from all of these homoeoids as the width of the homoeoids $\Delta\zeta$ becomes infinitesimally small $\Delta\zeta \rightarrow d\zeta$. The full integral in Schramm (1990) becomes rather messy and is re-formulated with slightly more elegance in Barkana (1998) as

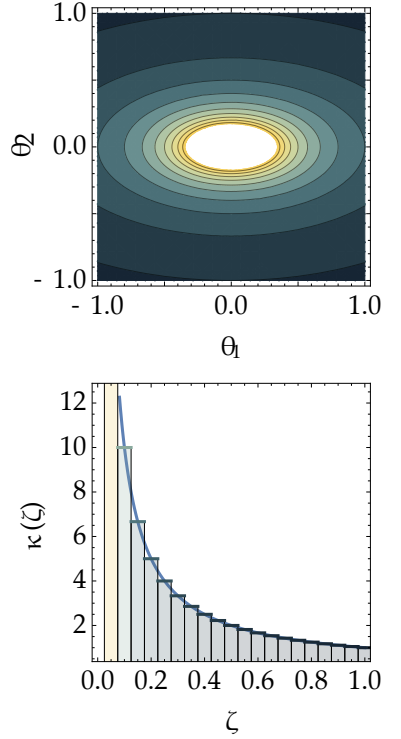


Figure 3.1: Homoeoidal slices of an elliptical lens. Note the top plot is in the angular coordinates of the image plane while the bottom plot is in elliptical coordinates.

² Consider again the differences between homoeoids and confocals in figure 2.8. The equipotential surfaces are similar ellipses close to \mathcal{H} . As we move away from \mathcal{H} it starts to look more like a point mass and the equipotential surfaces become circles, as we might expect.

$$\alpha_1(\theta_1, \theta_2) = 2\theta_1 \cos \beta' \int_0^{\zeta(\theta_1, \theta_2)} d\zeta' \frac{\zeta' \kappa(\zeta')}{\theta_1^2 + \omega^4 \theta_2^2} \omega \quad (3.5)$$

$$\alpha_2(\theta_1, \theta_2) = 2\theta_2 \cos \beta' \int_0^{\zeta(\theta_1, \theta_2)} d\zeta' \frac{\zeta' \kappa(\zeta')}{\theta_1^2 + \omega^4 \theta_2^2} \omega^3 \quad (3.6)$$

where $\zeta(\theta_1, \theta_2)$ is the elliptical radius at (θ_1, θ_2) , the axis ratio is now $f = \cos \beta'$, and we have used the definitions;

$$\omega^2 = \frac{\Delta + r^2 + \zeta^2 \sin^2 \beta'}{\Delta + r^2 - \zeta^2 \sin^2 \beta'}, \quad (3.7)$$

and

$$\Delta^2 = (\zeta'^2 \sin^2 \beta' + \theta_2^2 - \theta_1^2)^2 + 4\theta_1^2 \theta_2^2. \quad (3.8)$$

where $r^2 = \theta_1^2 + \theta_2^2$. The upper limit of the integral is $\zeta(\theta_1, \theta_2)$ because all the homoeoids outside the point of interest have no effect on the deflection angle at this point. Barkana points out that conveniently we can restrict our calculations to the first quadrant, where $\theta_1, \theta_2 > 0$, without any loss of generality. This helps to speed up computation by only making the calculations necessary in the first quadrant of the grid which can then be appropriately transformed into the other three quadrants.

The key modification in Barkana (1998) is the following change of variables for the deflection angle³. If we define a new variable μ , such that

$$\mu = \frac{\zeta'^2 \sin^2 \beta' + \theta_2^2 - \theta_1^2}{2\theta_1 \theta_2}, \quad (3.9)$$

then ω^2 factorises as

$$\omega^2 = \left[\mu + (\mu^2 + 1)^{1/2} \right] \frac{\theta_1}{\theta_2}. \quad (3.10)$$

Changing the variable in the mass distribution such that $\kappa(\zeta) \equiv \bar{\kappa}(\mu)$ gives much simpler integrands in the deflection angle. Now we have

$$\alpha_1(\theta_1, \theta_2) = \frac{\cos \beta' \sqrt{\theta_1 \theta_2}}{\sin^2 \beta'} \int_{\mu_1}^{\mu_2} d\mu \bar{\kappa}(\mu) g(\mu) \quad (3.11)$$

$$\alpha_2(\theta_1, \theta_2) = \frac{\cos \beta' \sqrt{\theta_1 \theta_2}}{\sin^2 \beta'} \int_{\mu_1}^{\mu_2} d\mu \bar{\kappa}(\mu) g(-\mu) \quad (3.12)$$

where,

$$g(\mu) = \sqrt{\frac{1}{\sqrt{1+\mu^2}} - \frac{\mu}{\mu^2+1}} \quad (3.13)$$

and the limits of integration are given by

$$\mu_1 = \frac{1}{2} \left(\frac{\theta_2}{\theta_1} - \frac{\theta_1}{\theta_2} \right), \quad \mu_2 = \frac{1}{2} \left(\frac{\theta_2}{\theta_1 \cos^2 \beta'} - \frac{\theta_1 \cos^2 \beta'}{\theta_2} \right). \quad (3.14)$$

This removes some of the complexity from the integrand and does improve computation speed. A preliminary implementation of the scheme was made using the calculations developed thus far. The

Here we use β' rather than Barkana's β to avoid confusion with the source plane coordinate

³ Note that this a function of the current integration variable ζ' and the coordinates θ_1 and θ_2 at which we are evaluating the integral.

method was tested against the analytic solutions for the SIE in [Kormann et al. \(1994\)](#), achieving accuracy up to floating point precision.

3.2 Truncating the Mass Distribution

With the desired accuracy achieved, we proceed to add the crucial part of the model. By truncating the mass distribution at a radius well inside the images, we ensure that any constraints achieved are solely due to the distribution of mass inside the images.

Before α can be calculated we will also need to define κ in terms of the new variable μ . Our original form for the mass distribution in terms of elliptical radius was

$$\kappa(\zeta) = \zeta^{1-\gamma}. \quad (3.15)$$

Using the definition of μ from equation 3.9, we can obtain ζ in terms of μ

$$\zeta = \frac{2\theta_1\theta_2 - \theta_2^2 + \theta_1^2}{\sin^2 \beta'} \mu, \quad (3.16)$$

which makes the mass distribution

$$\bar{\kappa}(\mu) = \left[\frac{2\theta_1\theta_2\mu - \theta_2^2 + \theta_1^2}{\sin^2 \beta'} \right]^{\frac{1}{2}(1-\gamma)}. \quad (3.17)$$

Chapter 2 showed that, at least in circular lenses, images are sensitive to the slope of the mass distribution **at the location of those images**.

In order to avoid our results being obscured by this fact, and to show that any constraints are only dependent on the mass distribution inside the images, we decide to truncate the mass distribution at a certain elliptical radius. This way, the parameters of the model can be set such that images form on the lens in **locations where they are far from any mass at all**.

This ensures that any sensitivity to the slope of the mass distribution is exactly that by allowing precise control over the location of the critical curve and the total mass within the lens.

To do this, we define a step function $\Theta_a(\mu)$ where

$$\Theta_a(\mu) = \begin{cases} \bar{\kappa}(\mu) & \frac{2\theta_1\theta_2\mu + \theta_1^2 - \theta_2^2}{a^2 \sin^2 \beta'} < 1.0 \\ 0 & \frac{2\theta_1\theta_2\mu + \theta_1^2 - \theta_2^2}{a^2 \sin^2 \beta'} \geq 1.0 \end{cases} \quad (3.18)$$

where a is the semi-major-axis of the ellipse at the truncation radius ζ_0 . To ensure some level of continuity when changing the ellipticity ϵ of the lens, the geometric mean of the semi axes of the bounding ellipse was kept constant. For a given ζ_0 , a and b were changed such that \sqrt{ab} remained the same while ϵ changed.

Having constructed a mass distribution that works in the integral and constrains all the mass to within an ellipse far from the images, we need to ensure that the total mass in this ellipse remains the same

even as γ and ϵ change. For a given comparison between two lenses with different parameters, this keeps the **radius** of the critical curve the same.

To do this, we preface the entire deflection angle calculation with a normalisation constant M_0 which is the total mass in the lens found via the integral over the area of the bounding ellipse in the first quadrant:

$$M_0(a, b, \gamma) = 4 \int_0^a \int_0^{\theta'_2} d\theta_2 d\theta_1 \left(\theta_1^2 + \theta_2^2 \frac{a^2}{b^2} \right)^{\frac{1}{2}(1-\gamma)} \quad (3.19)$$

where the limit of integration in the θ_2 direction is given by

$$\theta'_2 = b \left[1 - \left(\frac{\theta_1}{a} \right)^2 \right]^{\frac{1}{2}} \quad (3.20)$$

The first of the two integrals here does have an analytic solution with the exact form

$$M_0(a, b, \gamma) = 4 \int_0^a d\theta_1 b \theta_1^{-\gamma} \sqrt{1 - \frac{\theta_1^2}{a^2}} {}_2F_1 \left(\frac{1}{2}, \frac{1}{2}(\gamma-1); \frac{3}{2}; 1 - \frac{a^2}{\theta_1^2} \right) \quad (3.21)$$

where ${}_2F_1(a, b; c, z)$ is the hypergeometric function. With the above, $M_0(a, b)$ becomes easy to evaluate using SciPy's `special.hyp2f1` and `integrate.quad` functions.

Putting the above together we get

$$\bar{\kappa}(\mu) = \frac{M}{M_0(a, b, \gamma)} \Theta_a(\mu) \left[\frac{2\theta_1 \theta_2 \mu - \theta_1^2 + \theta_2^2}{\sin^2 \beta'} \right]^{\frac{1}{2}(1-\gamma)}, \quad (3.22)$$

which is now the final form of the mass distribution; a power law elliptical profile with

- A slope γ
- An axis ratio $f = \cos \beta'$
- Confined to an ellipse with semi-axes a and b
- Normalised by M_0 such that the total mass within the ellipse is M for any γ or f

The total mass M is set by the user and changes the radius of the critical curve (the Einstein radius)

3.3 Implementation and Discretisation

Having defined the necessary calculations, we can now summarise the actual implementation of the method. We define a two-dimensional grid of $N \times N$ pixels that covers the first quadrant of the image plane. The location of pixel i, j is specified by two coordinates x_{ij} and y_{ij} . The coordinate is placed in the middle of the pixel so as to avoid the problematic divergence of $\kappa(\zeta)$ when $x_{ij} = 0$ or $y_{ij} = 0$. The grid is

See [Weisstein \(2016\)](#) for the full definition.

defined on the interval $[0, 1]$ in both directions, meaning each pixel has a width $\Delta x = \Delta y = 1.0/N$.

For the specified parameters M , f and γ , the deflection angle is calculated. First we define a mass distribution using a function `mass_setup` which returns an **anonymous** function `kappa`⁴. This is the full mass distribution as defined in section 3.2 and at this stage is a function only of the integration variable.

We can define a grid of integration limits U_{1ij} and U_{2ij} as

$$U_{1ij} = \frac{1}{2} \left(\frac{y_{ij}}{x_{ij}} - \frac{x_{ij}}{y_{ij}} \right) \quad U_{2ij} = \frac{1}{2} \left(\frac{y_{ij}}{x_{ij} \cos^2 \beta'} - \frac{x_{ij} \cos^2 \beta'}{y_{ij}} \right) \quad (3.23)$$

In such calculations, the whole grid is treated like an algebraic variable by NumPy. Operations are performed element-wise and in many cases have been optimised to be much faster than looping over the grid and performing the calculations ‘manually’. A grid of normalisation constants Q_{ij} is calculated by

$$Q_{ij} = \frac{M}{M_0(a, b, \gamma)} \frac{\cos \beta' \sqrt{x_{ij} y_{ij}}}{\sin^2 \beta'}. \quad (3.24)$$

Finally, we loop over the grid and calculate each component of the deflection angle in each pixel using the numerical integration function `integrate.quad` from SciPy. This function is not vectorised and so computation slows down at this stage, optimisations are discussed in the next section. The deflection angle components are found element-wise by

$$\alpha_{1ij} = Q_{ij} \int_{U_{1ij}}^{U_{2ij}} du \bar{\kappa}(u) f(u), \quad (3.25)$$

$$\alpha_{2ij} = Q_{ij} \int_{U_{1ij}}^{U_{2ij}} du \bar{\kappa}(u) f(-u). \quad (3.26)$$

The grid is then redefined to cover the full interval $[-1, 1]$ in both directions and the deflection angle calculated in the first quadrant is translated into the other four quadrants.

Nine examples of deflection angle fields are plotted in figure 3.2, all created by the process described in this section. These nine examples span the extremes of the γ, f parameter space and show the very different deflection profiles that different parameters can produce. In all examples, the mass profile is truncated at an elliptical radius $\zeta = 0.3$ and the geometric mean of the semi-axes \sqrt{ab} is constant.

Steeper slopes have the effect of pulling mass inward and the deflection angle field begins to look more like a point mass, quite obvious in the $\gamma = 2.5$ cases. At the other extreme, $\gamma = 1.5$ leaves the mass much more spread out and the deflection angle is less sensitive to location. In some cases we can see the magnitude $|\alpha|$ decreasing once well inside the mass, a consequence of Newton’s theorem that only the mass internal to a homoeoid can provide an attractive force.

⁴ An anonymous function is a function within a program that is defined dynamically at the point of execution, rather than explicitly defined in the code. This allows the function to be passed as a variable to other functions and is especially useful for numerical integration.

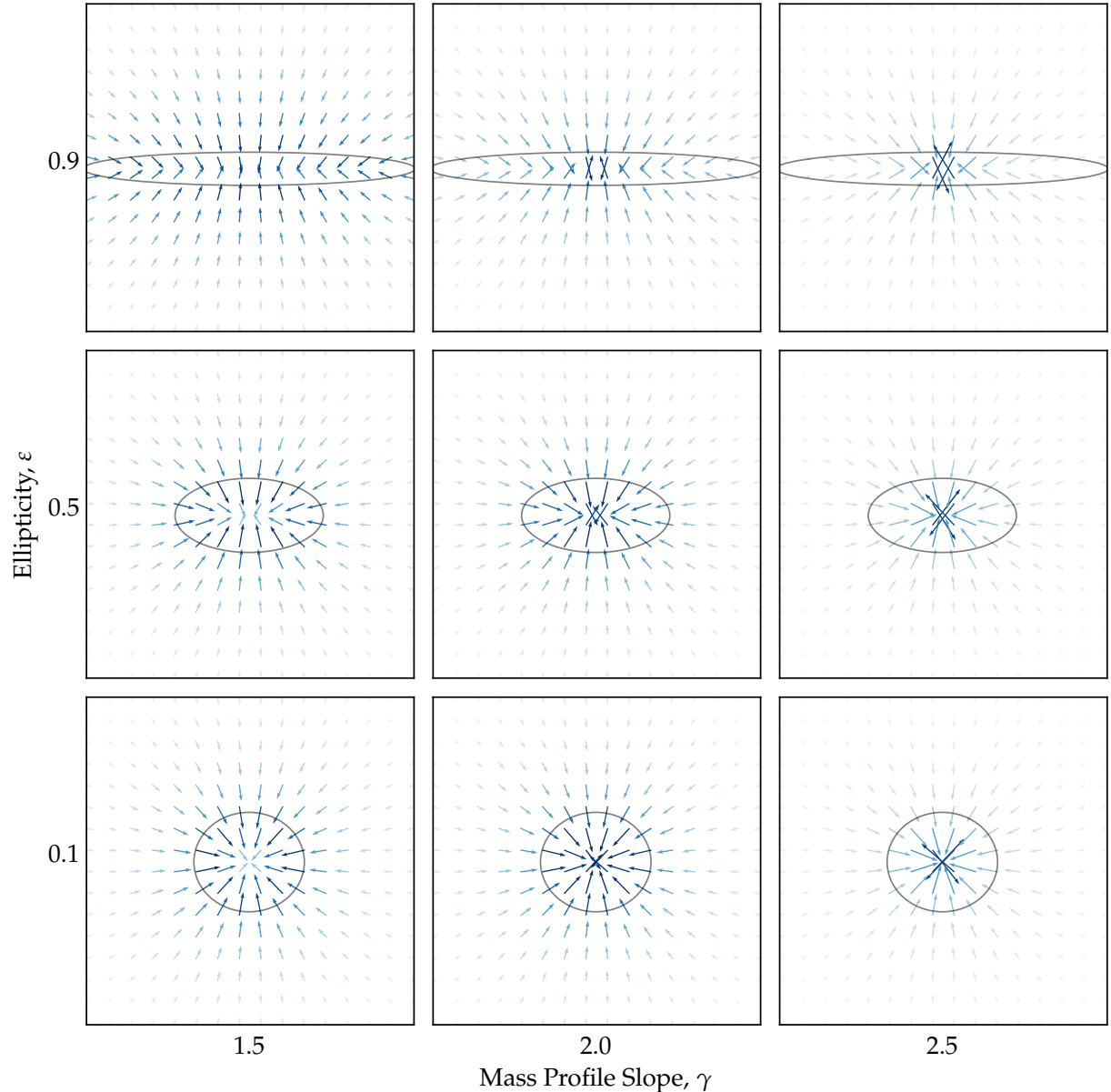


Figure 3.2: Examples of deflection angle fields from nine points in the γ, ε parameter space. The vectors are coloured according to the magnitude $|\alpha|$ of the deflection angle at that point.

3.4 Computation Speed and Optimisation

The preceding calculations are somewhat time-consuming. Almost all of the computation time is spent evaluating the integral for each pixel. For our purposes the calculations as presented here were quick enough although, for much larger grids there are a number of modifications that might be worthwhile.

Before significant time was spent calculating deflection angle fields for various parameter spaces, a feature was added to save the deflection angle field as a file once calculated, named according to the parameters used. Before any calculation a list could be checked by the program to see if those parameters had been used before and if they had, the deflection angle would be loaded from the file, dispensing with any computation time at all.

Early on in the project, a single run of 1600 calculations for a 40×40 grid on the γ, f parameter space produced all the deflection angle fields necessary for the results in the next section which freed up time for reduction and analysis. The process would adapt very well to parallelisation with different sets of parameters running simultaneously in their own routines, rather than in large loops over the parameter space.

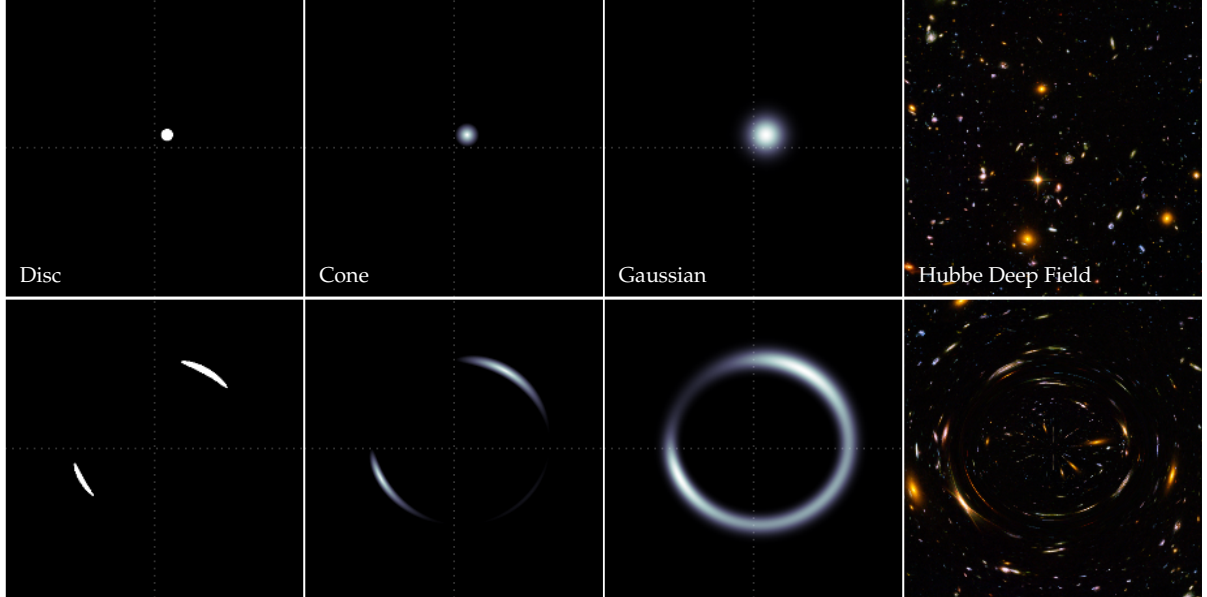
Significant improvements to speed are made in [Barkana \(1998\)](#), who goes on to add approximations to the integrand for desired degrees of accuracy by expanding $g(\mu)$ into a series of Chebyshev polynomials or approximating them by other means depending on the integration limits.

These further modifications bring significant improvements in computation time (20 times faster) for calculating the magnification tensor and the gravitational potential of the lens. The implementation of these improvements requires a feature for determining which of the optimisation routines is necessary given the integration limits and the current location on the grid. As these specific calculations were not necessary for this work, the extensions weren't made.

A much simpler, but cruder, improvement to speed can be made by simply checking the images produced by a small sample of parameter values before calculating the deflection angle at all values. The location of images in the samples would roughly define the area of interest on the image plane over the entire parameter space, and the calculation of deflection angle in areas where no images would ever form is then unnecessary and can be excluded from loops. For example, for most of the images used to produce results here, calculating the deflection angle was completely unnecessary for about 75% of the image plane. Occasionally this method was useful for quick, ad-hoc calculations but is not recommended for constructing complete results.

3.5 Defining Sources

The program allowed for sources to be input directly as image files (which have produced most of the images so far) or as functions; brightness profiles defined in terms of the source position coordinate β . Figure 3.3 shows three different sources constructed from functions; a solid disc, a cone, a Gaussian, and just for illustration, a real image taken from the Hubble Deep Field.



The images in figure 3.3 now differ slightly from the ones we saw in figure 2.10. This is due to the truncation of the mass profile. Even at $\epsilon = 0.5$, the images appear more circular than one might expect but there is a simple explanation.

Recall that the potential surface around a homoeoid is a series of **confocals** (see fig. 2.8). By truncating the profile at a certain radius, the equipotentials beyond that radius will become circles quicker than for an un-truncated elliptical lens. The deflection angle outside the lens then takes an intermediate form between that of a circular lens and an elliptical lens. At very high ellipticities this effect is less pronounced (see the highly elliptical examples in 3.2).

Figure 3.3: Four different methods of source construction, imaged by a $\gamma = 2.0, \epsilon = 0.5, M = 0.5, \zeta_0 = 0.3$ lens. In each the source is slightly off-axis. The deflection angles used here are those in figure 3.2 which included the truncated mass distribution.

3.6 Constructing Images

Putting together the final image created by the lens is a process called **ray-tracing**, and is the final physical step in the process. It simply involves mapping each of the pixels on the image plane back to a pixel on the source plane. We extract the value of the source for that pixel and add it to the image.

For a functional source this is quite easy. If the source's brightness profile is described by the function $B(\beta)$ then the brightness profile

of the image is simply $B(\theta - \alpha(\theta))$. For a pixelised source there is an extra step in translating source plane coordinates to actual pixel indices so that the value of the source in that pixel can be extracted. Rays that do not hit the grid are set to zero brightness.

3.7 Comparing Images

With a complete method for calculating the deflection angle and constructing images, it was now possible to compare images for slight changes in parameters. Measuring the sensitivity to these changes in parameters allowed us to place statistical constraints on the mass distribution and ellipticity. In this final section we describe the method for doing these comparisons.

First we construct an image of a source using a set of lens parameters γ_0 , ε_0 , ζ_0 and M . We will call the image I_0 which is a grid of the brightness values in each pixel, I_{0ij} . We then find an annulus on the lens plane which encloses all the lensed images between its two radii r_1 and r_2 . The number of pixels in this annulus is n .

The integrated signal to noise ratio (SNR) in the annulus is given by

$$\text{SNR} = \sum_{i,j}^{\text{Ann.}} \frac{I_{0ij}}{S_{ij}\sqrt{n}} \quad (3.27)$$

where S is the noise in each pixel. The values in S are drawn from a normal distribution $\mathcal{N}(0, \sigma_s)$ where σ_s is set such that $\text{SNR} = 30$. In general, the images used to model lenses in the literature have $50 \lesssim \text{SNR} \lesssim 120$ so our $\text{SNR} = 30$ is quite conservative. For justification on this, see similar arguments made in [Nightingale and Dye \(2015\)](#).

Having set the necessary amount of noise, a new image I_1 is created by adding the noise to the original image

$$I_{1ij} = I_{0ij} + S_{ij} \quad (3.28)$$

I_1 is now our simulated observation of the lens.

We now generate a series of model images I_k , each with its own set of parameters. We test the model images I_k against the original image I_1 by calculating χ^2 for each I_k ;

$$\chi^2 = \sum_{ij} \left[\frac{I_{1ij} - I_{kij}}{\sigma_s} \right]^2. \quad (3.29)$$

Many I_k are compared across the parameter space and we build up values of χ^2 . We then find the minimum on this χ^2 surface, χ_0^2 and subtract it from all values to obtain a new surface of $\Delta(\chi^2) = \chi^2 - \chi_0^2$.

This surface represents the statistical distance of each model image I_k from the original image I_1 in the parameter space. The contour around the minimum on this surface where $\Delta(\chi^2) = 1.0$ gives approximately the 68% confidence level or the 1σ error on the parameters. For a more detailed explanation of this, see section 15.6 in [Press et al. \(1992\)](#).

4 Results

In this chapter we present the constraints obtained on γ in the γ, ε parameter space for different lens and source parameters. The results show that overall, useful constraints can be placed on γ using lensing alone with a similar degree of accuracy to that achieved by the other studies in chapter 1. We also find that the size of these constraints varies significantly with the other parameters. The results here are provided without explanation, which will be conducted in detail in the next chapter.

For each section we define the model parameters used and briefly describe the results. The constraints themselves are shown as surfaces of $\Delta(\chi^2)$, calculated via the process in section 3.7. The value of $\Delta(\chi^2)$ at a particular point on any of the surfaces, is the value of $\Delta(\chi^2)$ between the original image, and a model created with the parameter values at that point on the surface.

In all cases the mass distribution is truncated at $\zeta_0 = 0.3$ and the source is a circular cone with a brightness of 1.0 at its centre, falling linearly to zero at a width of w . The image resolution used was 200×200 . For ease of comparison, all plots in this section use the same colour and contour scale.

Any quantitative description of the constraints are given here as estimates to one significant figure, derived from fitting a quadratic to a slice through the $\Delta(\chi^2)$ surface at $\Delta(\chi^2) = 0$. A more rigorous statistical analysis will be needed before conclusive results can be obtained, not only for finding the size of the constraints, but also because the images are generated with random noise, and constraints can vary slightly on repeated attempts.

4.1 Constraints on Total Mass

Firstly, we show that the total mass M is very well constrained. We place a source of width $w = 0.05$ (5% of the diameter of the image plane) on the optical axis and image it with a lens of $\gamma_0 = 2.0$ and $\varepsilon_0 = 0.5$. Images are then created by adjusting total mass M around its original value of 1.0 and adjusting γ across the interval [1.5, 2.5]. The constraints on M and γ in this situation are plotted in figure 4.1. The constraints are elliptical and we find $\sigma_\gamma \sim 0.02$ and $\sigma_M \sim 10^{-3}$.

4.2 Constraints on γ at Different Ellipticities

Now we swap the mass parameter M for the ellipticity ε and follow the same process. Using the same source as before with three lenses of $\gamma_0 = 2.0$ and $\varepsilon_0 = 0.4, 0.5$ and 0.6 , we change ellipticity across the interval $[0.1, 0.9]$. These constraints are shown for each ε_0 in figure 4.2.

Quadratic fits through the $\Delta(\chi^2)$ surface are shown in figure 4.3. To properly define the constraints on γ or ε here, we would need to marginalise over the second parameter. As an estimate from fitting we give the constraints in table 4.1.

4.3 Constraints on γ with Different Source Positions

All the sources imaged so far have been on the optical axis. As we saw in figure 2.10 there are significant changes in image structure as a source leaves the optical axis. We now briefly consider the effect on our constraints that this movement will have. Using the same lens parameters as before ($\gamma_0 = 2, \varepsilon_0 = 0.5$) we now move the source and compare the constraints on γ and ε for sources positioned at a radial distance of $r_s = 0.05, 0.1$ and 0.2 from the optical axis. These results are shown in figure 4.4 and estimates for the size of the constraints are printed in table 4.2.

4.4 Constraints on γ with Different Source Sizes

We know place the source back on the optical axis and examine the change in constraints with the size of the source. Again, using a lens with $\gamma_0 = 2, \varepsilon_0 = 0.5$ we adjust the source width w and observe the changes in our constraints on γ and ε . These constraints for sources with $w = 0.1$ and 0.2 are shown in figure 4.5.

ε_0	σ_γ	σ_ε
0.4	0.20	0.03
0.5	0.04	0.01
0.6	0.02	0.01

Table 4.1: Estimates for the size of the 1σ uncertainty on γ and ε for the constraints in fig. 4.2.

r_s	σ_γ	σ_ε
0.00	0.04	0.01
0.05	0.03	0.01
0.10	0.04	0.02
0.20	<0.01	<0.01

Table 4.2: Estimates for the size of the 1σ uncertainty on γ and ε for the constraints in fig. 4.4.

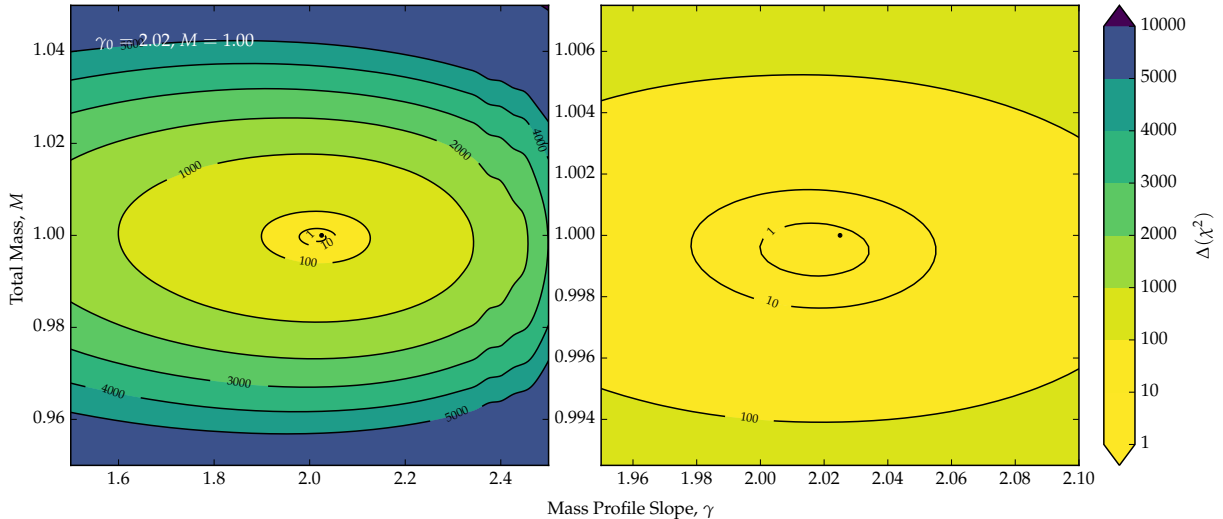


Figure 4.1: The $\Delta(\chi^2)$ surface for M and γ around an original image with $\gamma_0 = 2$ and $M = 1.0$. The minimum (best fit) is found at $\gamma_0 = 2.02, M = 1.0$. The total mass is constrained to within $\sigma = 10^{-3}$.

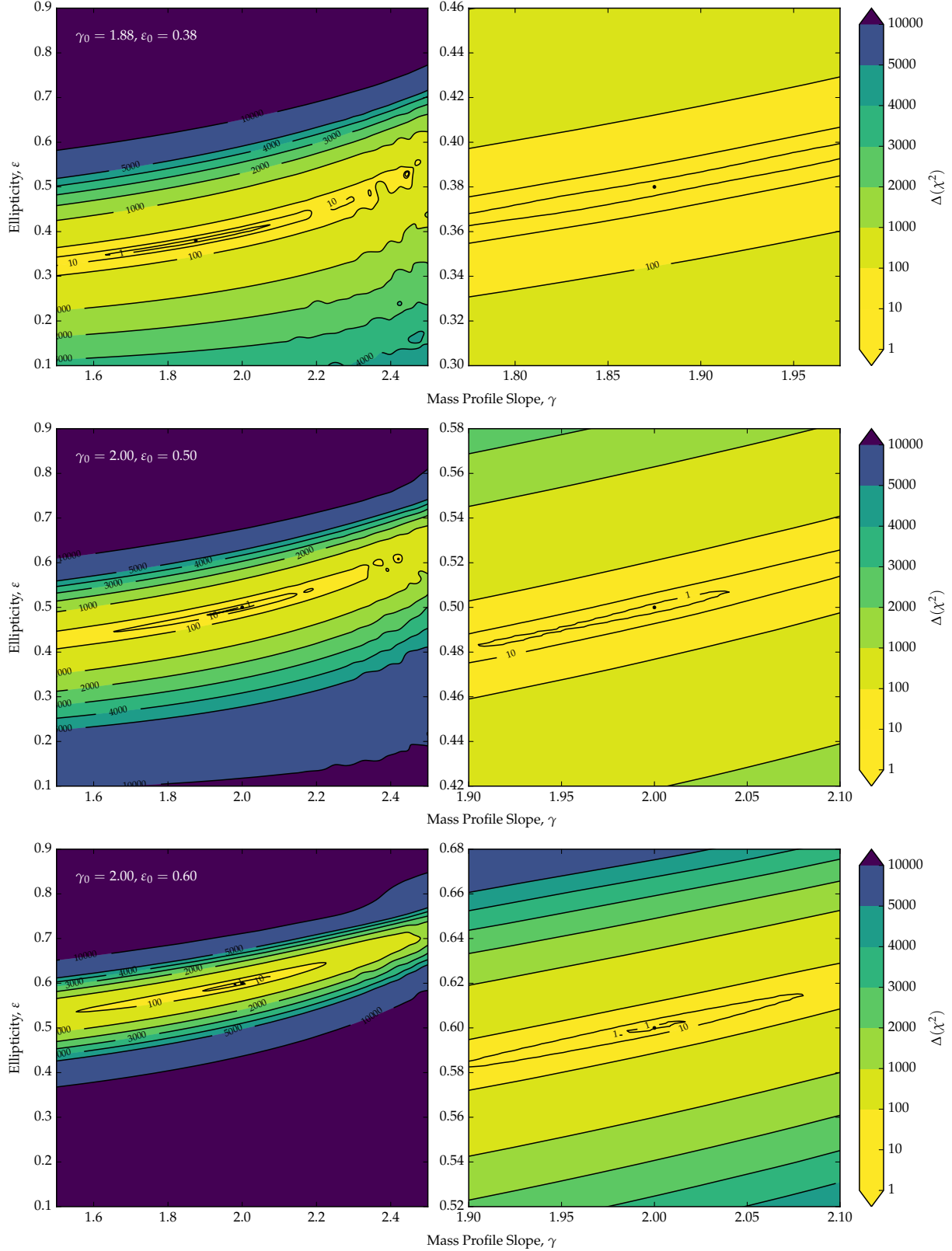


Figure 4.2: The $\Delta(\chi^2)$ surface for ε and γ around original images with $\gamma_0 = 2$ and $\varepsilon_0 = 0.4, 0.5$ and 0.6 . The constraints on both γ and ε become much better as ellipticity increases.

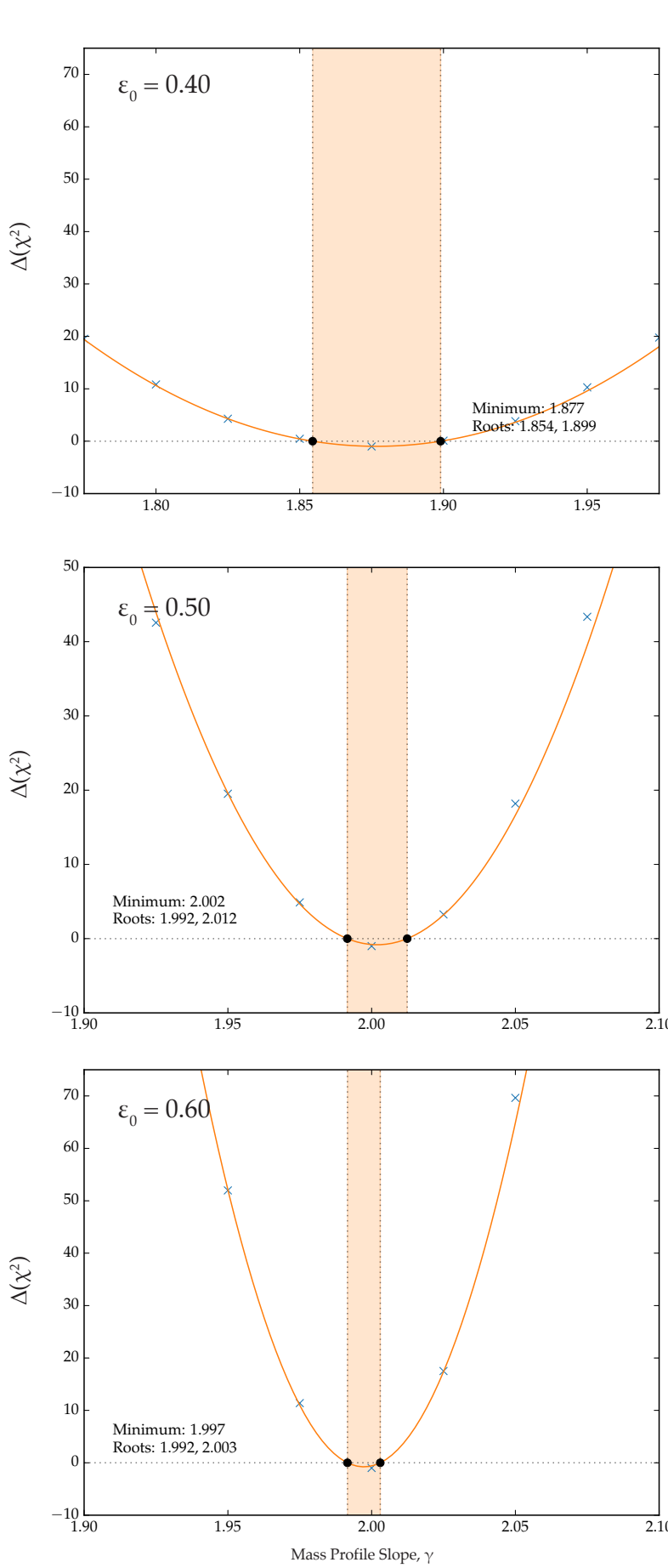


Figure 4.3: Slices through the $\Delta(\chi^2)$ surface along γ at the three minimum values of ε found in figure 4.2. The blue crosses are the closest few $\Delta(\chi^2)$ values to the minimum and the orange line is a quadratic fit to these data. The roots of the curve $\Delta(\chi^2) - 1$ give the 1σ error on γ , indicated by the shaded region.

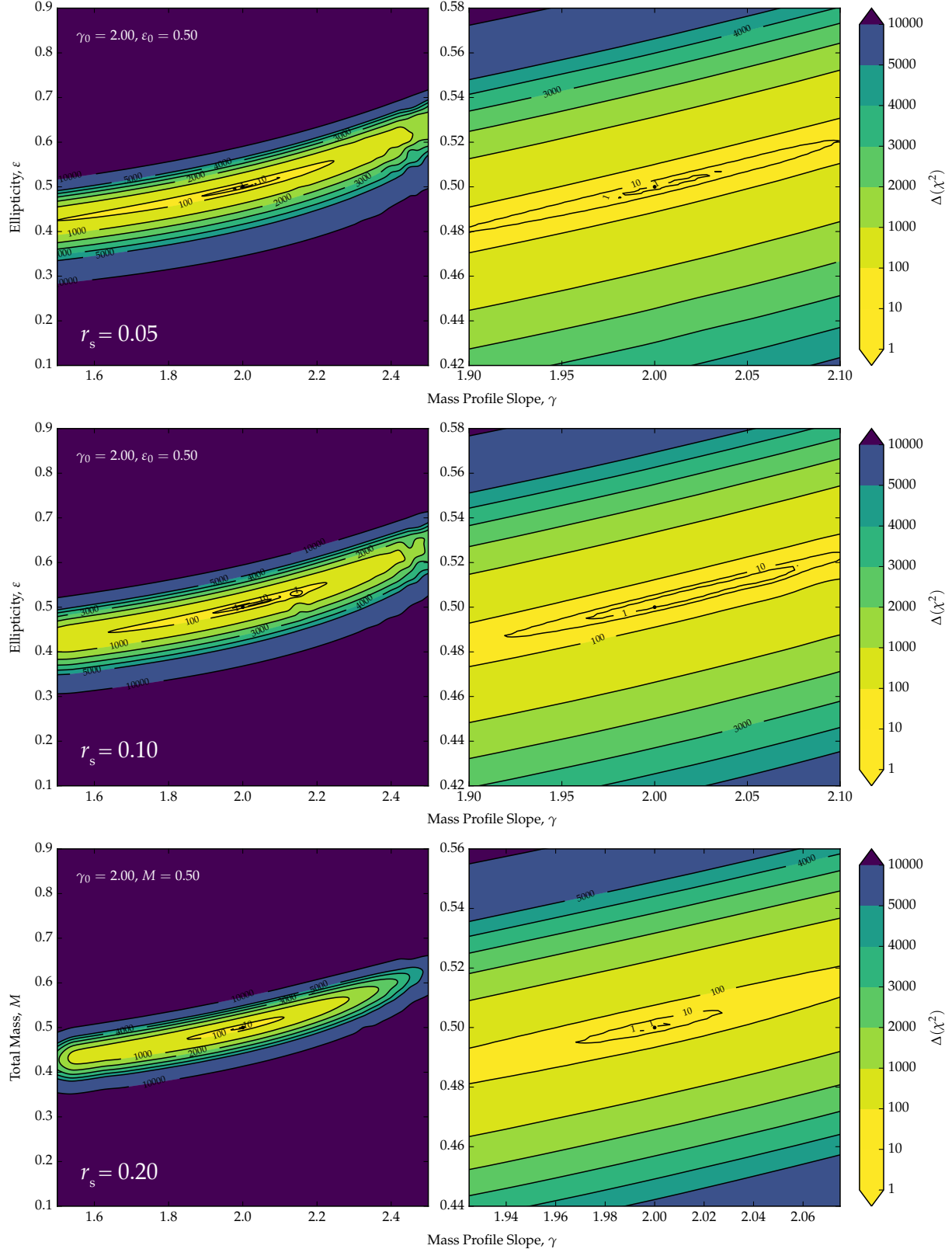


Figure 4.4: The $\Delta(\chi^2)$ surface for ε and γ around original images with $\gamma_0 = 2$, $\varepsilon_0 = 0.5$ and source positions $r_s = 0.05, 0.1, 0.2$. Compare with the $r_s = 0$ case in the centre plot of fig. 4.2. Constraints improve as the source moves away from the optical axis.

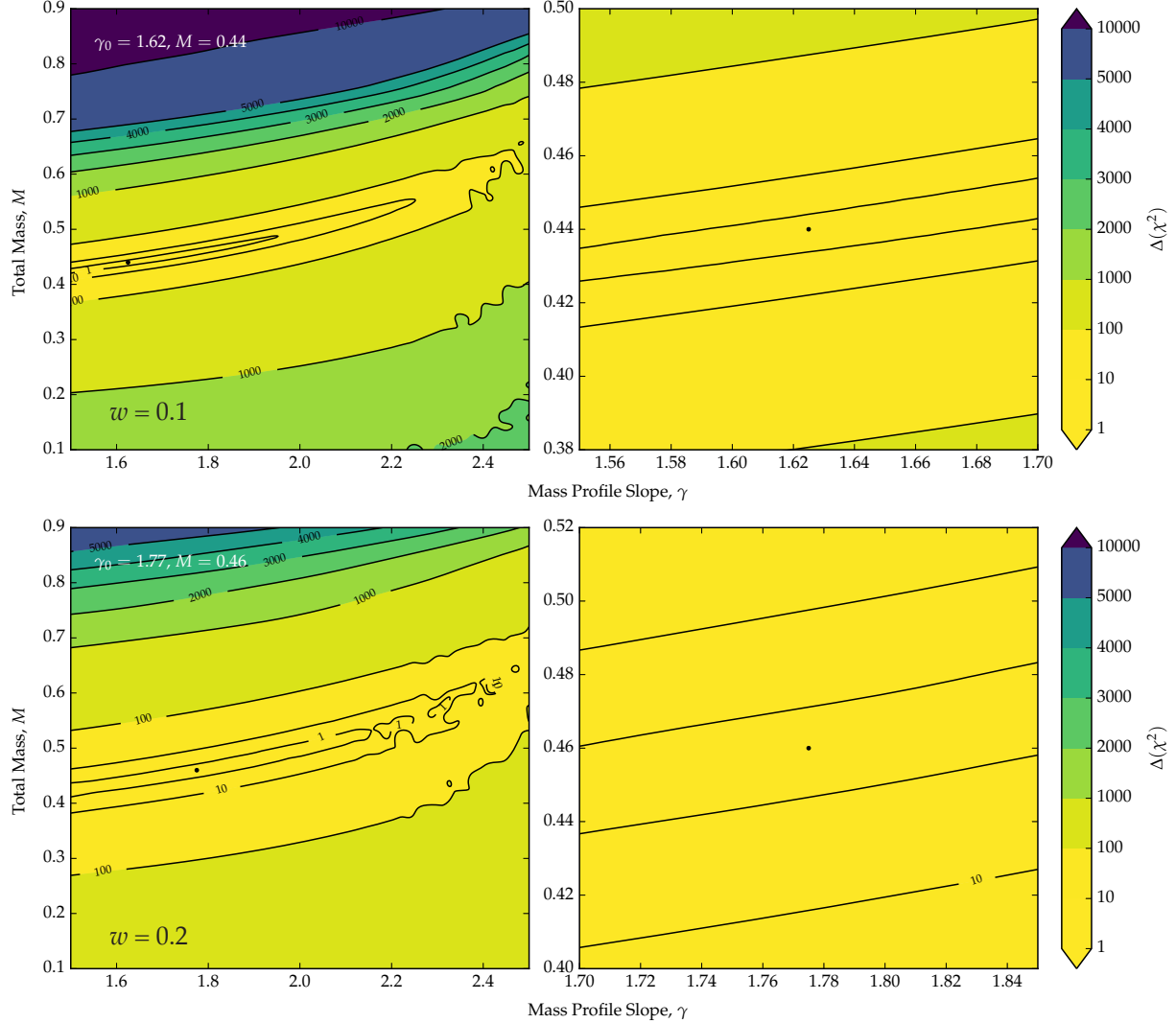


Figure 4.5: The $\Delta(\chi^2)$ surface for ε and γ around original images with $\gamma_0 = 2$, $\varepsilon_0 = 0.5$ and source widths $w = 0.1, 2.0$. Compare with the $w = 0.05$ case in the centre plot of fig. 4.2. Constraints deteriorate as the source expands.

5 Discussion and Conclusions

This section will roughly concern two different subjects. The first is a discussion of the results themselves, especially their validity and the nature of any degeneracies that we have found. The second is a discussion of the project more generally, including explanations for choices in method, and an outline of potential future improvements. We finish with a summary of the key results.

5.1 Degeneracies and Validity of Results

Defining any truly qualitative result at this stage would be premature. Rather, the success of the project so far is in finding the size and shape of the constraints and the degeneracies between parameters in a more general sense. In time, a better statistical analysis coupled with more intensive computation will provide these results and quantify the constraints in the many-dimensional parameter space of the lensing model.

All results in the previous chapter show a well constrained ellipticity, suggesting that angular structure is an excellent provider of information for lensing models. There is still however a significant degeneracy between γ and ε in all circumstances. This does make physical sense; as γ increases and the lens becomes more like a point mass, the lost angular structure can be restored by increasing ellipticity. At lower ellipticities (see the $\varepsilon_0 = 0.38$ plot in fig. 4.2) this degeneracy becomes debilitating to the point that the model cannot constrain γ to any useful degree. This same degeneracy is found in similar size and shape by [Nightingale and Dye \(2015\)](#) whose results are reproduced in figure 5.1.

We have seen that the constraints are also quite sensitive to the properties of the source. This points to other degeneracies between γ and the source parameters which will be worth further investigation. A significant degeneracy between γ and the source position likely exists. For the more elliptical lenses, the cut and caustic on the source plane are sensitive to the mass profile. Changing their location would be the same as changing the source position, in terms of the images produced.

It is less clear how significant a degeneracy would be between source size and γ . The source begins to negatively effect the constraints as it starts to cover the caustic. An increase in γ would reduce the size of the caustic in an elliptical lens, thereby making it

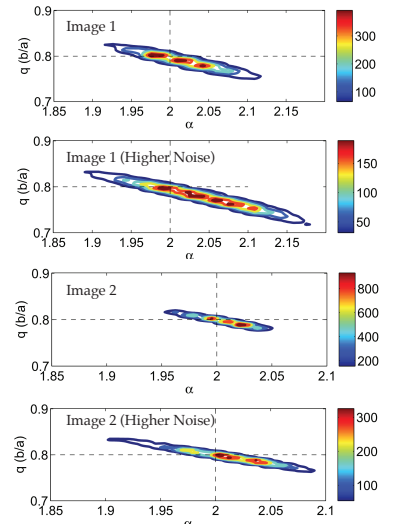


Figure 5.1: The full two-dimensional probability density function (PDF) on γ and ε from [Nightingale and Dye \(2015\)](#) for two different images, each with a version with higher noise. Note that the axis ratio $q = b/a$ is used here rather than $\varepsilon = 1 - q$.

easier for a small source to produce a ring if it lies near the optical axis. In this way, increasing source size and increasing γ may have an identical effect on images, producing a degeneracy.

5.2 Limitations of Method

Although encouraging results have been produced, there are many possible improvements to be made. The limiting factor in any extension to the work already presented would be the intense computation required to produce any results. For example, the $\Delta(\chi^2)$ surface in figure 4.2 is a grid of 40×40 combinations of γ and ε . To produce an image at each combination requires the calculation of the deflection angle on a 100×100 grid. This amounts to the evaluation of the integral in equation 3.25 some 16×10^6 times. If the deflection angle field for one image can be evaluated in a minute (an optimistic estimate), the entire computation still takes over 24 hours.

Improvements may be possible using the approximations in [Barkana \(1998\)](#) if the truncation of the mass distribution is properly accounted for. Focusing on smaller areas of the parameter space would also cut down on computation, now that the nature of the constraints are much clearer. Better computation speed would be used to improve the resolution of the γ, ε grid, or indeed to produce grids on any other parameter space, thus improving measurements of the size of the constraints.

5.3 Statistical Analysis

Once computation has been improved, the most valuable extension would be a more robust and conclusive analysis of the $\Delta(\chi^2)$ surfaces in the previous chapter. The obvious choice for this would be the Bayesian approach developed in [Suyu et al. \(2006\)](#) and later used by many lensing studies for parameter estimation. See [Auger et al. \(2010\)](#), [Barnabe et al. \(2011\)](#) or [Nightingale and Dye \(2015\)](#) for examples of this.

Along with this technique, a more complete parameter space would bolster the results. The ideal method would include the mass profile slope, the ellipticity, the source size and position, and the mass in one single parameter space. Estimates on parameters would be found from MCMC sampling the $\Delta(\chi^2)$ surface and producing a full posterior probability distribution over all parameters, before marginalising to find the constraints on a single parameter.

Also of interest is the **detail** of the source. If structure is observed within the source there is more information for the lens to image and this may well have a significant effect on the constraints.

The mass-sheet degeneracy (see section 2.6) would also warrant consideration in a more complete analysis. The truncation and normalisation used here leaves the mass interior to the bounding ellipse unchanged and a change in source position can not account for a change in image structure under these circumstances. However,

if the effect of truncation itself was considered as a parameter, the mass-sheet degeneracy would become more important.

5.4 Summary of Key Results

Our results show that meaningful constraints on the mass profile can certainly be achieved from lensing alone, **even when the mass is entirely enclosed by the images**. Across all the results it is clear that sources and lenses with less symmetry produce the best constraints. We have demonstrated that an elliptical lens model can succeed where, as we have already shown, a circular model would always fail.

We observe that, as expected, the **total mass** of the lens is very well constrained, more so than any other parameter we considered (fig. 4.1). The total mass within a lens dictates its Einstein radius, the most important element of the image structure in a lens.

Changing the mass by only small amounts changes the convergence, κ in the lens but does not effect the shear η . This has the simple effect of moving images inwards or outwards isotropically, leaving little overlap between images of similar but numerically different mass.

The constraints show a sensitivity to the **ellipticity of the lens** itself with higher ellipticities producing better constraints (fig. 4.2 and 4.3). This is explained by the fact that lenses of higher ellipticity produce images with greater angular structure. In lenses with little angular structure, images of the same source will only vary along the radial direction between similar lenses. The angular structure at high ellipticities gives the images an extra dimension along which variation can be produced, thereby improving constraints (see fig. 2.10 and 3.2).

Also of importance is the **position of the source** with sources just off the optical axis producing better constraints than those on the axis (fig. 4.4). Again, this result is explained by considerations of symmetry. Consider again the behaviour of images as a source moves off the optical axis in figure 2.10. On the axis we see two pairs of two identical images. Two of the images in this case are not actually adding any new information to the lens plane as they are just copies of the other two. Moving off the axis breaks the symmetry and we now see three or four images that are entirely different. This symmetry breaking adds new information and thus better constraints.

Although it hasn't been shown here, we should expect that a source moving radially away from the axis would see improving constraints on parameters until it reached the caustic (see fig. 2.9). As it crosses the caustic, two of the images are lost. With less source information now in the lens plane we would expect the constraints to stop improving at the caustic where they would begin to deteriorate until the source was no longer being distorted by the lens, providing no constraints at all.

Finally, we have also observed a strong dependence on the **size**

of the source. In figure 4.5 where $w = 0.1$ and 0.2 the constraints are at least an order of magnitude larger than in the other figures where $w = 0.05$ (a more realistic size). We can explain this result by considering the caustic structure of plots I through VI in figure 2.10. The caustic of the truncated lens used in the results likely has a size somewhere between that of plots III and IV. Such a caustic will become partially covered for a $w = 0.1$ source and fully covered with $w = 0.2$. At this point an elliptical ring is formed, creating significant symmetry in the image plane and making constraints more difficult.

Bibliography

- Auger, M. W., Treu, T., Bolton, A., Gavazzi, R., Koopmans, L. V. E., Marshall, P. J., Moustakas, L. A., and Burles, S. (2010). The sloan lens acs survey x. stellar, dynamical and total mass correlations of massive early-type galaxies. *ApJ*, 724.
- Barkana, R. (1998). Fast calculation of a family of elliptical gravitational lens models. *ApJ*, 502.
- Barnabe, M., Czoske, O., Koopmans, L. V. E., Treu, T., and Bolton, A. (2011). Two-dimensional kinematics of slacs lenses - iii. mass structure and dynamics of early-type lens galaxies beyond $z \sim 0.1$. *MNRAS*, 415.
- Bolton, A., Burles, S., Koopmans, L. V. E., Treu, T., and Moustakas, L. A. (2006). The sloan lens acs survey i. a large spectroscopically selected sample of massive early-type lens galaxies. *ApJ*, 638.
- Bonvin, V., Courbin, F., Suyu, S. H., Marshall, P. J., and Rusu, C. E. (2016). New cosmograil time delays of he 0435-1223. *MNRAS*, (Submitted).
- Chandrasekhar, S. (1969). *Ellipsoidal Figures of Equilibrium*. Yale University Press.
- Coe, D., Zitrin, A., Carrasco, M., Shu, X., Zheng, W., and Postman, M. (2013). Clash: Three strongly lensed images of a candidate $z \approx 11$ galaxy. *ApJ*, 762.
- Courteau, S., Cappellari, M., de Jong, R., Dutton, A., Emsellem, E., Hoekstra, H., Koopmans, L., Mamon, G., Maraston, C., Treu, T., and Widrow, L. (2014). Galaxy masses. *Rev. Mod. Phys.*, 86.
- Dutton, A. A. and Treu, T. (2013). The bulge-halo conspiracy in massive elliptical galaxies: implications for the stellar initial mass function and halo response to baryonic processes. *arXiv:1303.4389*.
- Dye, S., Negrello, M., Hopwood, R., Nightingale, J. W., Bussmann, R. S., Amber, S., Bourne, N., Cooray, A., Dariush, A., Dunne, L., Eales, S. A., Nuevo, J. G., Ibar, E., Ivison, R. J., Maddox, S., Valiante, E., and Smith, M. (2014). Herschel-atlas: Modelling the first strong gravitational lenses. *MNRAS*, 440.
- Dye, S., Smail, I., Swinbank, A. M., Ebeling, H., and Edge, A. C. (2007). Separation of the visible and dark matter in the einstein ring lbgj213512.73-010143. *MNRAS*, 379.

- Dye, S. and Warren, S. J. (2005). Decomposition of the visible and dark matter in the einstein ring 0047-2808 by semilinear inversion. *ApJ*, 623.
- Falco, E. E., Gorenstein, M. V., and Shapiro, I. I. (1985). On mode-dependent bounds on h_0 from gravitational images: Application to q0957+561a,b. *ApJ*, 289.
- Kochanek, C. S. (1991). The implications of lenses for galaxy structure. *ApJ*, 373.
- Kochanek, C. S., Schneider, P., and Wambsganss, J. (2004). Gravitational lensing: Strong, weak & micro. In *Proceedings of the 33rd Saas-Fee Advanced Course*.
- Koopmans, L. V. E. and Treu, T. (2003). The structure and dynamics of luminous and dark-matter in the early-type lens galaxy of 0047-281 at $z = 0.485$. *ApJ*, 583.
- Koopmans, L. V. E., Treu, T., Bolton, A., Burles, S., and Moustakas, L. A. (2006). The sloan lens acs survey iii. the structure and formation of early-type galaxies and their evolution since $z = 1$. *ApJ*, 649.
- Kormann, R., Schneider, P., and Bartelmann, M. (1994). Isothermal elliptical gravitational lens models. *A&A*, 284.
- Linder, E. V. (2011). Lensing time delays and cosmological complementarity. *Phys. Rev. D*.
- Naryan, R. and Bartelmann, M. (1995). Lectures on gravitational lensing. In *Formation of Structure in the Universe*, Proceedings of the Jerusalem Winter School.
- Nightingale, J. W. and Dye, S. (2015). Adaptive semi-linear inversion of strong gravitational lens imaging. *MNRAS*, 452.
- Press, W. H., Teukolsky, S. A., Vetterling, W. T., and Flannery, B. P. (1992). *Numerical Recipes in Fortran 77: The Art of Scientific Computing*. Cambridge University Press.
- Schneider, P. and Sluse, D. (2013). Mass-sheet degeneracy, power-law models and external convergence: impact on the determination of the hubble constant from gravitational lensing. *A&A*, 559.
- Schramm, T. (1990). Realistic elliptical potential wells for gravitational lens models. *A&A*, 231.
- Schramm, T. (1994). A toolbox for general elliptical gravitational lenses. *A&A*, 284.
- Shu, Y., Bolton, A., Mao, S., and Kochanek, C. S. (2016). The boss emission line lens survey iv: Smooth lens models for the bells gallery sample. *ApJ (Submitted)*.

Suyu, S., Marshall, P. J., Hobson, M., and Blandford, R. (2006). A bayesian analysis of regularized source inversions in gravitational lensing. *MNRAS*, 371.

Suyu, S. H., Marshall, P. J., Auger, M. W., Hilbert, S., Koopmans, L. V. E., and Treu, T. (2010). Dissecting the gravitational lens b1608+656 ii. precision measurements of the hubble constant, spatial curvature and the dark energy equation of state. *ApJ*.

Treu, T. (2010). Strong lensing by galaxies. *Annu. Rev. Astron. Astrophys.*, 48:87–125.

Walsh, D., Carswell, R. F., and Weymann, R. J. (1979). 0957+561 a, b: twin quasistellar objects or gravitational lens? *Nature*, 279.

Warren, S. J. and Dye, S. (2003). Semilinear gravitational lens inversion. *ApJ*, 590.

Weisstein, E. W. (2016). [WolframMathWorld: The Hypergeometric Function](#).

Willis, J. P., Hewett, P. C., Warren, S. J., Dye, S., and Maddox, N. (2006). The ols-lens survey: The discovery of five new galaxy-galaxy strong lenses from the sdss. *MNRAS*, 369.